

1 **The impact of recent changes in South Asian anthropogenic emissions of SO₂ on sulfate**
2 **loading in the upper troposphere and lower stratosphere and the associated radiative**
3 **changes**

4 Suvarna Fadnavis¹, Rolf Müller², Gayatry Kalita¹, Matthew Rowlinson², Alexandru Rap², Jui-
5 Lin Frank Li³, Blaž Gasparini⁴ Anton Laakso⁵

6 ¹Indian Institute of Tropical meteorology, Pune, India²

7 Forschungszentrum Jülich GmbH, IEK7, Jülich, Germany

8 ³School of Earth and Environment, University of Leeds, Leeds, UK.

9 ⁴Jet Propulsion Laboratory, California Institute of Technology, Pasadena, California, USA

10 ⁵Department of Atmospheric Sciences, University of Washington, Seattle, USA

11 ⁶Finnish Meteorological Institute, Finland

12 Corresponding author: suvarna@tropmet.res.in

13 Abstract:

14 Convective transport plays a key role in aerosol enhancement in the upper troposphere
15 and lower stratosphere (UTLS) over the Asian monsoon region where low-level convective
16 instability persists throughout the year. We use the state of art ECHAM6–HAMMOZ global
17 chemistry-climate model to investigate the seasonal transport of anthropogenic Asian sulfate
18 aerosols and their impact on the UTLS. [Sensitivity simulations for SO₂ emission perturbation](#)
19 [over India \(48 % increase\) and China \(70 % decrease\) are performed based on the Ozone](#)
20 [Monitoring Instrument \(OMI\) satellite observed trend; rising over India by ~4.8 % per year](#)

21 and decreasing over China by ~ 7.0 % per year during 2006 – 2017. The enhanced Indian
22 emissions result in an increase in Aerosol Optical Depth (AOD) loading in the UTLS by 0.61
23 to 4.17 % over India. These aerosols are transported to the Arctic during all seasons by the
24 lower branch of the Brewer-Dobson circulation enhancing AOD by 0.017 % to 4.8 %.
25 Interestingly, a reduction of SO₂ emission over China inhibits the transport of Indian sulfate
26 aerosols to the Arctic in summer-monsoon and post-monsoon seasons due to subsidence over
27 northern India. The region of sulfate aerosols enhancement show significant warming in the
28 UTLS over North India, South China (0.2±0.15 to 0.8±0.72 K) and the Arctic (~1±0.62 to
29 1.6±1.07 K). The estimated seasonal mean direct radiative forcing at the top of the atmosphere
30 (TOA) induced by the increase in Indian SO₂ emission is -0.2 to -1.5 W·m⁻² over northern
31 India. The Chinese SO₂ emission reduction leads to a positive radiative forcing of ~0.6 to 6
32 W·m⁻² over China. The decrease in vertical velocity and the associated enhanced stability of
33 the upper troposphere in response to increased Indian SO₂ emissions will likely decrease
34 rainfall over India.

35 Keywords: sulfate aerosols, radiative forcing, upper troposphere, and lower stratosphere,
36 India, China.

37

38 **1. Introduction**

39 Emissions of sulfur dioxide (SO₂) were shown to have large detrimental effects on air
40 quality, and therefore, human health. Moreover, increases in SO₂ have effects on the
41 hydrological cycle and crop yield (Li et al., 2017; Shawki et al., 2018). On the other hand, SO₂
42 emissions have a cooling effect on climate, due to the increased formation of sulfate aerosols
43 (SO₄²⁻) which are produced from the oxidation of SO₂. Over the Asian region, the high
44 emission growth of SO₂ also has implications on the recurrent and more severe droughts
45 happening during the second half of the twentieth century resulting in socio-economic impacts
46 (Kim et al., 2016; Paul et al., 2016; Zhang et al., 2012a). Its effects on precipitation deficit is
47 via scattering of solar radiation leading to the invigoration of surface cooling, reduction in
48 land-ocean thermal contrast, and overturning of circulation (Ramanathan et al., 2005, Yeh et
49 al.,2015; Shawki et al., 2018).

50 To curb its adverse effect, implementation of international legislation on sulfur
51 emission was enforced which resulted in global decrease until 2000 followed by a sharp rise
52 until 2006 and declining trend afterward. The global rising and declining trend seem to be
53 modulated by the emissions from China since it is the world largest SO₂ emitting country
54 (Aas et al., 2019). While SO₂, emissions over China have declined since 2006 (by ~75%),
55 India shows a continued increase (~50%) (Krotkov et al., 2016; Li et al., 2017). The rising
56 trend in SO₂ emissions in India is due to sustained economic growth during the last few
57 decades (Krotkov et al., 2016). According to the Indian Ocean Experiment (INDOEX) during
58 January to March 1999 sulfate aerosols over the Indian region contribute 29 % to the observed
59 aerosol optical depth (AOD) (Verma et al., 2012). [The Aerosol Radiative Forcing over India](#)
60 [NETwork \(ARFINET\) AOD](#) measurements over India show a consistent rising annual trend of

61 0.004 during 1988 – 2013 (Babu et al., 2013). Over North India sulfate AOD estimates vary
62 between ~ 0.10 and 0.14 , and the direct radiative forcing (DRF) at TOA between ~ -1.25 to
63 and $-2.0 \text{ W}\cdot\text{m}^{-2}$ (Verma et al., 2012). Globally, the current best estimate of sulfate aerosol
64 DRF is $-0.4 \text{ W}\cdot\text{m}^{-2}$ ($-0.6 \text{ W}\cdot\text{m}^{-2}$ to $-0.2 \text{ W}\cdot\text{m}^{-2}$) (Myhre et al., 2013).

65 The long-range transport of sulfate aerosols from the Asian boundary layer to the UTLS
66 and further northward to the Arctic ([poleward](#) of 65°N) alter the aerosol burden in the upper
67 troposphere over Asia and the Arctic (Bourgeois and Bey, 2011; Yang et al., 2018). This
68 northward extending layer from Asia to the Arctic in the UTLS affects the surface temperature
69 and produces climatic impacts via DRF (Yang et al., 2018). The Cloud-Aerosol Lidar with
70 Orthogonal Polarization (CALIOP) satellite measurements and model simulations indicate that
71 13 % (annual mean) of the sulfate in the Arctic troposphere comes from Asia (Bourgeois and
72 Bey, 2011). The model sensitivity experiments for 20 % emission reduction of SO_2 show a
73 decrease in the sulfate aerosol burden in the Arctic by $\sim 36 - 41$ % when tagged with East
74 Asian emission and $\sim 7 - 10$ % in response to South Asian emissions. The global burden of
75 sulfate aerosols during 1975 – 2000 has produced a cooling trend of $0.02 \text{ K decade}^{-1}$ in
76 surface temperature (Yang et al., 2018). The recent significant changes in SO_2 emissions
77 within Asia are likely to alter the atmospheric burden of sulfate aerosols and their impacts (on
78 radiative forcing, clouds, temperature etc.), both regionally and at the remote locations.

79 The transport of aerosols from the Asian boundary layer to the UTLS by the monsoon
80 convection is known to form and maintain the Asian Tropopause Aerosols Layer (ATAL)
81 ([SPARC-ASAP, 2006](#); Fadnavis et al., 2013; Vernier et al., 2015; Yu et al., 2017; Vernier et
82 al., 2018). In the future, the aerosol burden in the UTLS may increase due to rising trends in
83 aerosol emission. The enhancement in the UTLS involves complexities due to transport

84 processes. Previous work indicates that a fraction of Asian emissions is transported to the
85 UTLS (contributing to the ATAL associated with the monsoon anticyclone) since the majority
86 of aerosols that grow into cloud droplets (~80 %) is removed by precipitation. Two-thirds of
87 the total aerosol loading that reach the monsoon anticyclone is transported poleward through
88 circulation in the lower stratosphere (Lelieveld et al., 2018). The observed SO₂ concentrations
89 in the monsoon anticyclone are ~5 – 10 times higher than in the rest of the tropics (Lelieveld et
90 al., 2018). The major sources of aerosols in the ATAL are found in India and China, with
91 Indian emissions dominating the composition of the ATAL (Lau et al., 2018). Climate model
92 simulations show that the Asian monsoon region (15 – 45 °N, 30 – 120 °E) is three times more
93 efficient (per unit area and time) in enhancing aerosol in the Northern Hemisphere stratosphere
94 than annually - averaged tropical (15 °N – 15 °S) upwelling (Yu et al., 2017). Although the
95 chemical composition of the particles constituting the ATAL is not well understood, satellite
96 observations (e.g. Cloud-Aerosol Lidar and Infrared Pathfinder Satellite Observation,
97 CALIPSO; Stratospheric Aerosol and Gas Experiment, SAGE-II; balloonsonde and aircraft
98 measurements (e.g. Civil Aircraft for the Regular Investigation of the atmosphere Based on an
99 Instrumented Container; CARIBIC) suggest that ATAL particles may contain large amounts
100 of sulfate, as well as black carbon, organic, nitrates (including ammonium nitrate) and dust
101 (Vernier et al., 2015; 2018; Yu et al., 2016; Höpfner et al., 2019). Further, model studies
102 suggest sulfate is, together with organics, as a major chemical component of the ATAL (e.g.,
103 Fadnavis et al., 2013; Yu et al., 2017). However, there is also a model study (Gu et al., 2016)
104 that emphasizes the importance of nitrate as a chemical component of the aerosol in the UTLS
105 over the Tibetan Plateau and the South Asian summer monsoon region. In addition, balloon
106 measurements from Hyderabad, India indicate the presence of large amounts of nitrate

107 aerosols near the tropopause (100 ng m^{-3}), which may be due to NO_x from anthropogenic
108 emissions, lightning, and gas-to-aerosol conversion (Vernier et al., 2015; 2018). Further, Yu et
109 al. (2016, 2017) report that sulfate and nitrate aerosols are important components of the
110 ATAL. Aerosol loadings in the UTLS result in a significant impact on radiative forcing. For
111 example, satellite observations show that the ATAL layer has exerted a regional radiative
112 forcing at the top of the atmosphere of approximately $-0.1 \text{ W}\cdot\text{m}^{-2}$ in the past 18 years, thus
113 locally reducing the impact of global warming (Vernier et al., 2015).

114 Over Asia, the intensity of seasonal convection is controlled by regional instability and
115 thereby modulating the horizontal and vertical transport processes (Luo, 2013). The transport
116 pathways of pollutants lifted into upper troposphere by the monsoon convection are well
117 documented: (i) quasi-isentropic transport in the monsoon anticyclone above about 360 K
118 from the monsoon anticyclone into the extra-tropical lowermost stratosphere, (ii) cross-
119 isentropic transport from the UTLS into the tropical stratosphere by slow, radiatively driven
120 ascent, and (iii) transport of air into the stratosphere by deep convection that sometimes
121 crosses the tropopause in the tropics (Kremser et al., 2016; Fadnavis et al., 2017a; Vogel et al.,
122 2019). However little is known about the transport of Asian pollutants in the UTLS outside of
123 the summer monsoon.

124 In this study, we address the following research questions: (1) what is the seasonal
125 contribution of SO_2 emissions from India and China to the AOD in the UTLS? (2) what is the
126 associated radiative forcing? (3) can the increase/decrease in Indian/Chinese SO_2 emissions
127 change the seasonal dynamics and clouds in the UTLS? For this purpose, we perform two sets
128 of sensitivity simulations based on observed satellite trends in SO_2 emissions over India (48 %

129 increase) and China (70 % decrease) during 2006 - 2017 using the state of art aerosol-
130 chemistry-climate model ECHAM6–HAMMOZ (version echam6.1.0-ham2.1-moz0.8).

131 The paper is organized as follows: Section 2 describes the model simulations and
132 measurements used in our study. The model evaluation follows in Section 3. The distribution
133 of aerosols in the UTLS is discussed in Section 4. The impact of sulfate aerosols on radiative
134 forcing, cloud ice, and temperature are presented in Section 5. Discussions are given in section
135 6. Finally, section 7 presents the conclusions of this study.

136

137 **2. Measurements and model simulations**

138 **2.1 Satellite and ground-based measurements of AOD**

139 We analyze aerosol retrievals from Multi-Angle Imaging Spectroradiometer (MISR)
140 (level-3 version 4, at 550 nm wavelength during 2000 – 2016) (Martonchik et al., 2002), The
141 MISR AOD measurements give aerosol properties over the global ocean and land with bright
142 targets such as deserts (Kahn et al., 2001). Aerosol-Robotic-NETwork (AERONET) sun
143 photometer, level 2.0 version 3 daily AOD observations during 2006 – 2016 (Holben et al.,
144 1998) were also analyzed at the stations in the Indo–Gangetic Plain, (Bihar: 84.12 °E, 25.87
145 °N, Jaipur: 75.80 °E, 26.90 °N, Kanpur: 80.23 °E, 26.51 °N, Karachi: 67.13 °E, 24.95 °N),
146 and China (Xiang He: 39.76 °E, 11.00 °N, Nghia Do: 21.04°N, 105.80 °E).

147 **2.2 SO₂ measurements from the Ozone Monitoring Instrument (OMI)**

148 The Ozone Monitoring Instrument (OMI) aboard the NASA Aura spacecraft retrieves
149 SO₂ data from Earthshine radiances in the wavelength range of 310.5 – 340 nm (Levelt et al.,

150 2006). It gives the total number of SO₂ molecules in the entire atmospheric column above a
151 unit area (https://disc.gsfc.nasa.gov/datasets/OMSO2e_V003/). Details of the retrieval
152 technique are documented by Li et al., (2017). To understand the impact of SO₂ emission
153 changes over India and China, we estimate a trend in the SO₂ (2007 – 2017) over the Indian
154 region (70 – 95 °E, 8 – 35 °N) and the Chinese region (95 – 130 °E; 20 – 45 °N) (see Fig. 2e).
155 For this purpose, we used version 1.3, level-2, OMI retrievals that assume all SO₂ is located in
156 the planetary boundary layer. We use a regression model described by Fadnavis and Beig
157 (2006). A model regression equation is given as follows:

$$158 \theta(t,z) = \alpha(z) + \beta(z) \text{Dayindex}(t) \quad (1)$$

159 where $\theta(t,z)$ is the daily mean number of SO₂ molecules averaged over the Indian/Chinese
160 region, with altitude z set to 1 km, as we use column data. The model uses the harmonic
161 expansion to calculate the seasonal coefficient, α , and the trend coefficient, β . The harmonic
162 expansion for $\alpha(t)$ is given as:

$$163 \alpha(t) = A_0 + A_1 \cos \omega t + A_2 \sin \omega t + A_3 \cos 2\omega t + A_4 \sin 2\omega t \quad (2)$$

164 Where $\omega = 2\pi/12$; A_0, A_1, A_2, \dots are constants and t ($t=1,2, \dots,n$) is the time index. The
165 estimated trend value for SO₂ is $4.8 \pm 3.2 \text{ \% yr}^{-1}$ over the Indian region and $7.0 \pm 6.3 \text{ \% yr}^{-1}$
166 over the Chinese region (**significant at 99 % confidence level**). These trend values are used
167 while designing the model sensitivity simulations (discussed in section 2.4).

168

169

170 **2.3 CloudSat and Cloud-Aerosol Lidar Infrared Pathfinder Satellite Observations** 171 **(CALIPSO)**

172 We use the ice water content (IWC) dataset from a combination of CALIPSO lidar and
173 CloudSat radar data (2C-ICE dataset, version L3_V01) for the period 2007 – 2010 (Deng et
174 al., 2013). The Cloud Profiling Radar (CPR) onboard the CloudSat satellite is a 94 GHz nadir-
175 looking radar which measures the power backscattered by clouds as a function of distance. It
176 provides information on cloud abundance, distribution, structure, and radiative properties. The
177 Cloud-Aerosol Lidar with Orthogonal Polarization (CALIOP) is an elastically backscattered
178 active polarization-sensitive lidar instrument onboard CALIPSO. CALIOP transmits laser
179 light simultaneously at 532 and 1064 nm at a pulse repetition rate of 20.16 Hz. The lidar
180 receiver subsystem measures backscatter intensity at 1064 nm and two orthogonally polarized
181 components of 532 nm backscatter signal that provide the information on the vertical
182 distribution of aerosols and clouds, cloud particle phase, and classification of aerosol size
183 (Winker et al., 2010). The details of the data retrieval method are explained in Li et al. (2012).

184 **2.4 The model simulations**

185 The ECHAM6-HAMMOZ aerosol-chemistry-climate model used in the present study
186 comprises of the ECHAM6 global climate model coupled to the two moment aerosol and
187 cloud microphysics module HAM (Stier et al., 2005; Tegen et al., 2019) and the sub-model for
188 trace gas chemistry MOZ (Kinnison et al., 2007). HAM predicts the nucleation, growth,
189 evolution, and sinks of sulfate (SO_4^{2-}), black carbon (BC), particulate organic matter (POM),
190 sea salt (SS), and mineral dust (DU) aerosols. The size distribution of the aerosol population is
191 described by seven log-normal modes with prescribed variance as in the M7 aerosol module

192 (Stier et al., 2005; Zhang et al., 2012b). Moreover, HAM explicitly simulates the impact of
193 aerosol species on cloud droplet and ice crystal formation. Aerosol particles can act as cloud
194 condensation nuclei or ice nucleating particles. Other relevant cloud microphysical processes
195 such as evaporation of cloud droplets, sublimation of ice crystals, ice crystal sedimentation,
196 detrainment of ice crystals from convective cloud tops, etc. are simulated interactively
197 (Lohmann and Ferrachat, 2010; Neubauer et al., 2014). The anthropogenic and fire emissions
198 of sulfate, BC, and OC are based on the AEROCOM-ACCMIP-II emission inventory for the
199 study period 2010 – 2011 (Textor et al., 2006). The MOZ sub-model describes the trace gas
200 chemistry from the troposphere up to the lower thermosphere. The species included within the
201 chemical mechanism are contained in the O_x , NO_x , HO_x , ClO_x , and BrO_x chemical families,
202 along with CH_4 and its degradation products. Several primary non-methane hydrocarbons
203 (NMHCs) and related oxygenated organic compounds are also included. This mechanism
204 contains 108 species, 71 photolytic processes, 218 gas-phase reactions, and 18 heterogeneous
205 reactions on aerosol (Kinnison et al., 2007). Details of anthropogenic, biomass burning,
206 biogenic, emissions fossil fuel sources, etc. are reported by Fadnavis et al. (2017a).

207 The model simulations are performed at the T63 spectral resolution corresponding to
208 $1.875^\circ \times 1.875^\circ$ in the horizontal dimension, while the vertical resolution is described by 47
209 hybrid σ -p levels from the surface up to 0.01 hPa. The model has 12 vertical levels in the
210 UTLS (50 – 300 hPa). The simulations have been carried out at a time step of 20 minutes.
211 AMIP sea surface temperature (SST) and sea ice cover (SIC) (Taylor et al., 2000) were used as
212 lower boundary conditions. We performed 10-member ensemble runs by varying the initial
213 conditions (both SST and SIC) starting between 1 and 10 January 2010 and ending on 31
214 December 2011 to obtain statistically significant results. The analysis is performed for the year

215 2011. The 2011 Indian monsoon was well within the long term norm, with no strong
216 influences from the Indian Ocean Dipole or El Niño modes of inter-annual climatic variability.
217 We refer to it as the control simulation (CTRL). In previous work, Fadnavis et al. (2013;
218 2017b) used the ensemble means from 6–10 members to analyze the variability of aerosols
219 and associated impacts during the monsoon season. In two emission sensitivity simulations we
220 have applied (1) a flat 48% increase in anthropogenic SO₂ emissions over India (referred to as
221 Ind48 simulation) and, (2) a flat 48% increase in anthropogenic SO₂ emissions over India and
222 a flat 70 % decrease in anthropogenic SO₂ emissions over China simultaneously, (referred to
223 as Ind48Chin70 simulation); same assumptions for simulated years. The simulation design is
224 based on the estimated trend of 4.8 % per year over India and -7.0 % over China, from OMI
225 SO₂ observations during 2007 – 2017. The Ind48 and Ind48Chin70 simulations are also 10
226 member ensemble runs for the same period as CTRL and are analyzed for the year 2011 (see
227 Table-1). We compare the CTRL and Ind48, Ind48Chin70 simulations to understand the
228 seasonal impact of enhanced sulfate aerosol on the UTLS, radiative balance, and cirrus clouds.
229 We should mention that our simulations are canonical in design in order to show the impact of
230 Asian sulfate aerosols; they do not include many of the observed complexities, like radiative
231 forcing due to non-sulfate aerosols (e.g., organics, nitrates, and dust, etc.). [The QBO is not](#)
232 [internally generated in the model](#). Notwithstanding this, the present work provides valuable
233 insight into the relevance of the impact of sulfate aerosol originating from India and China on
234 the UTLS.

235 The seasons considered in this study are pre-monsoon (March-May), summer-
236 monsoon (June-September), post-monsoon (October-November), and winter (December-
237 February).

238 **2.5 Offline radiative calculations**

239 We use offline radiative calculations to explore the radiative impacts of enhanced
240 sulfate aerosol loadings in the UTLS only (300 – 50 hPa), compared to the all atmosphere
241 enhancement. Radiative effects associated with the sulfate aerosol enhancement are calculated
242 using the SOCRATES radiative transfer model (Edwards and Slingo, 1996; Rap et al., 2013)
243 with the CLASSIC aerosol scheme (Bellouin et al., 2011). We used the offline version of the
244 model with six shortwave and nine longwave bands, and a delta-Eddington two-stream
245 scattering solver at all wavelengths.

246

247 **3. Model evaluation with observations [via remote sensing](#)**

248 In [Figs. 1a–h](#), we show the distribution of seasonal mean cloud ice mixing ratio from
249 ECHAM6–HAMMOZ and combined measurements of total cloud ice from CloudSat and
250 CALIPSO (2C–ICE) (2007 – 2010). Although cloud ice is underestimated in the model (~6–
251 15 mg·kg⁻¹; 35–45%), the spatial distribution is well reproduced. Both the model simulations
252 and the observations show high amounts of cloud ice in the mid-upper troposphere (450 – 250
253 hPa) over the Asian monsoon region (80 – 120 °E). Cloud ice peaks during the monsoon
254 season with a second peak in the pre-monsoon season. The observed seasonality might have
255 linkages with seasonal transport process in the troposphere (details in section 4.2). The
256 differences in model simulations and observations are due to uncertainties in satellite
257 observations and model biases (Li et al., 2012); for example, the model does not consider large
258 ice particles unlike the cloud ice measurement from CloudSat and CALIPSO. The total ice
259 water mass estimates from 2C–ICE combine measurements from CALIPSO lidar

260 depolarization, which is sensitive to small ice particles (i.e., cloud ice represented in global
261 climate models), and CloudSat radar, which is very sensitive to larger ice particles (i.e.,
262 precipitating ice or snow) (Li et al., 2012).

263 Figures 2a-l shows the distribution of seasonal mean AOD from MISR (2000 – 2016),
264 model simulations (CTRL) and AERONET observations (2006 – 2016) (Bihar, Jaipur,
265 Kanpur, Karachi, XiangHe, NghiaDo). The model reproduces the large AOD over the Indo-
266 Gangetic Plains and Eastern China as seen in the MISR. However, simulated AOD is
267 underestimated in the model compared to MISR over the Indo-Gangetic Plains (~0.4) and
268 overestimated over Eastern China (~0.25). Comparison with AERONET observations also
269 shows underestimation in the model AOD over the stations in the Indo-Gangetic plains and
270 China (~0.23 – 0.35). The underestimation of model AOD over India and overestimation over
271 china in comparison with MISR is an agreement with ECHAM-HAMMOZ simulations in
272 Kokkola et al. (2018) and Tegen et al. (2019). The differences in the magnitude of AOD
273 between model, satellite remote sensing (MISR) and AERONET observations may be due to
274 various reasons, e.g., Satellite remote sensing detects AOD from top of the atmosphere while
275 AERONET detects AOD from the ground. Dumka et al. (2014) have documented that in
276 AERONET observations, the aerosols above 4 km contribute 50 % of AOD at Kanpur (in the
277 Indo-Gangetic plains). Inclusion of nitrate aerosol may affect the distribution of the AOD.
278 There are also uncertainties in model estimates of sea salt emission and parameterization
279 (Spada et al., 2013). The dust aerosols are underestimated the model (Kokkola et al., 2018).
280 The majority of CMIP5 models underestimate global mean dust optical depth (Pu and Ginoux,
281 2018). During the monsoon season, the large AOD values near 25 °N, 75 °E are likely due to
282 the presence of high amounts of sea salt and water-soluble aerosols in the model.

283 4. Results

284 4.1 A layer of aerosol in the UTLS

285 The Asian region (8 – 45 °N; 70 – 130 °E) experiences convective instability
286 throughout the year with a peak in the monsoon season (Manohar et al., 1999; Luo, 2013).
287 Distribution of seasonal mean outgoing longwave radiation, simulated ice crystal number
288 concentration, and cloud droplet number concentrations representing convection is shown in
289 Fig. S1. It depicts convection over the Asian region rising to the UT throughout the year and is
290 wide-spread during the monsoon season. The summer-monsoon convection lifts the boundary
291 layer aerosols to the upper troposphere, leading to the formation of the Asian Tropopause
292 Aerosol Layer (ATAL) (Fadnavis et al., 2013, Vernier et al., 2015). The CALIPSO lidar and
293 Stratospheric Aerosol and Gas Experiment II (SAGE-II) satellite observations reveal that the
294 ATAL extends over a wider Asian region (15 – 40 °N, 60 – 120 °E) between 12 –18 km
295 (Vernier et al., 2015; Fadnavis 2013).The ECHAM6-HAMMOZ simulations reproduce the
296 formation of an ATAL (extinction and sulfate aerosol) in the UTLS during the summer-
297 monsoon season (Figs. 3a-b). The aerosol layer in the UTLS is connected to the troposphere
298 during the pre-monsoon, indicating transport of tropospheric aerosols into the UTLS. From
299 March to November, the altitude of convective outflow propagates deeper into the UTLS.
300 Strong uplift during the summer-monsoon season lifts the mid-tropospheric aerosols and
301 aerosol precursors to the UTLS, generating aerosol minima in the mid-troposphere (Fadnavis
302 et al., 2013). During the summer-monsoon season, the convective transport mostly occurs
303 from the Bay of Bengal, the South China Sea and southern slopes of Himalayas (Fadnavis et
304 al., 2013; Medina et al., 2010). After the convective uplift, at altitudes above ~360 K,
305 radiatively driven upward transport in the anticyclonic monsoon circulation occurs at a rate of

306 $\sim 1 \text{ K}\cdot\text{day}^{-1}$; this is a slower uplift than convection but faster than outside the anticyclone
307 (Vogel et al., 2019). The simulated distribution of aerosol extinction and sulfate aerosols at
308 100 hPa from the CTRL simulation shown in Figs. 3c-d indicates [maxima in aerosol extinction](#)
309 (Fig. 2c) and sulfate aerosols (Fig. 2d) in the anticyclone region.

310 The estimated ratio of ECHAM6–HAMMOZ simulated sulfate aerosols in the UTLS to
311 the total aerosol amount is 6:10 pointing at sulfate aerosols as a major ATAL constituent.
312 Balloonsonde observations over South Asia also indicate that large amounts of sulfate aerosols
313 may be present in the ATAL (Vernier et al., 2015). [Tropospheric SO₂ and sulfate aerosol](#)
314 [transported into the stratosphere during volcanically quiescent periods are potentially large](#)
315 [contributors to the stratospheric aerosol burden \(SPARC-ASAP, 2006\).](#)

316 **4.2 Transport into the upper troposphere and lower stratosphere**

317 We investigate the transport pathways of sulfate aerosol during different seasons from
318 anomalies of sulfate aerosol for (1) Ind48, and (2) Ind48Chin70 simulations. Firstly, we
319 [present a vertical distribution of anomalies \(relative to CTRL\) of sulfate aerosol for Ind48](#)
320 simulations in Figs. 4 a-h. The striking feature is [poleward](#) transport of Indian emissions in the
321 UTLS throughout the year. A layer of sulfate aerosols enhancement extending from India to
322 the Arctic (68 – 90 °N), is seen near the tropopause, during pre-monsoon (3 – 15 $\text{ng}\cdot\text{m}^{-3}$) and
323 the lowermost stratosphere during summer-monsoon (2 – 15 $\text{ng}\cdot\text{m}^{-3}$), post-monsoon (2 – 6
324 $\text{ng}\cdot\text{m}^{-3}$) and winter (0.5 – 3 $\text{ng}\cdot\text{m}^{-3}$) seasons. [This layer may be due to transport of Indian](#)
325 [sulfate aerosols to the Arctic by the lower branch of the Brewer-Dobson circulation. These](#)
326 [sulfate aerosols enhance the AOD in the UTLS by 0.184E-04 \(i.e. 1.1%\) to 4.15E-04 \(i.e.](#)
327 [4.17%\) over India and the Arctic \(seasonal details in Table-2\).](#) Past studies also indicate the

328 transport of pollution from South Asia and East Asia to the Arctic predominantly in the UTLS
329 (Shindell et al., 2008; Fisher et al., 2011). From multi-model simulations, Shindell et al.
330 (2008) show that seasonally varying transport of south-Asian sulfate aerosols to the Arctic
331 maximizes in the pre-monsoon season. This enhancement of sulfate aerosols near the Arctic
332 maximizing during the pre-monsoon is also illustrated in Figure 4a.

333 Figure 4 also shows that during most seasons the vertical transport occurs from the Bay
334 of Bengal, Arabian Sea, southern slopes of Himalayas (60 – 100 °E; 15 – 35 °N), except
335 during the post-monsoon season when it occurs from the west Asia and Tibetan Plateau region
336 (20 – 35 °N; 60 – 75 °E; 75 – 95 °E). This may be due to the transport of sulfate aerosols from
337 the Indian region to these regions, which might have been lifted to the UTLS by the post-
338 monsoon convection (see Figs.S1 c, h, k, and S2 c). The enhancement of sulfate aerosols in the
339 monsoon anticyclone (an ATAL feature) and the cross-tropopause transport associated with
340 the summer monsoon convection is evident in Figs. 4c-d (enhancement $\sim 5 - 15 \text{ ng}\cdot\text{m}^{-3}$; 10 –
341 36 %). Past studies show that the aerosols transported into the lower stratosphere by the
342 monsoon convection are recirculated in the stratosphere by the lower branch of the Brewer-
343 Dobson circulation (Randel and Jensen, 2013; Fadnavis et al., 2013; Fadnavis et al., 2017b).
344 Yu et al., (2017) report that ~ 15 % of the Northern Hemisphere column stratospheric aerosol
345 originates from the Asian summer monsoon anticyclone region. Figure 4d shows that aerosols
346 spread to east and west from the anticyclone (20 – 120 °E), likely due to east/westward eddy
347 shedding from the anticyclone (Fadnavis and Chattopadhyay, 2017; Fadnavis et al., 2018).
348 Eddy shedding is not evident in the seasonal mean distribution (Fig. 3 b) due to its short
349 duration (i.e., days) and episodic nature.

350 The influence of the Chinese SO₂ emission reduction (Ind48Chin70) on the vertical
351 distribution of sulfate aerosols is shown in Figs 5a-h. In the pre-monsoon season, the transport
352 pattern is similar to the Ind48 simulations; however, the enhancement of sulfate aerosols at the
353 Arctic tropopause is significantly hindered (1 – 3 ng.m⁻³). The subsidence over north India (20
354 – 35 °N) has resisted sulfate aerosols crossing tropopause (Figs. 9 a, e). A feeble plume tilted
355 westward is seen during the monsoon season (Figs. 5c-d) and eastward-equatorward during
356 post-monsoon due to changes in circulations (ascending winds over south India and strong
357 subsidence over north India; Figs. 9 f-g). Entrainment into the anticyclone and cross-
358 tropopause transport of the sulfate aerosols, seen in the Ind48 simulation, is inhibited by this
359 subsidence. Interestingly, during summer-monsoon and post-monsoon seasons, poleward
360 transport of south Asian sulfate aerosols have also been cut-off due to circulation changes
361 (subsidence over north India see below in Figs. 9f-g). During winter, vertical winds over ~20
362 °N lifts aerosols from India to the mid-troposphere and further transported to the Arctic (Figs.
363 5 k-l, Fig. 9h). The vertical transport of sulfate aerosols increases AOD in the UTLS over
364 India by ~0.32E-04 (0.61 %) to 19.20E-04 (19.25 %) (except winter) and Arctic by 2.09E-04
365 (16.45 %) during the pre-monsoon season (see Table-2).

366

367 **5. Impact of changes in SO₂ emissions**

368 **5.1 Radiative forcing**

369 The seasonal mean anomalies of net radiative forcing at TOA due to sulfate aerosols
370 from the Ind48 and Ind48Chin70 simulations of the ECHAM6-HAMMOZ model are
371 illustrated in Figs. 6a-h. In general, both simulations show negative forcing over India and the

372 surrounding region where sulfate aerosols are dispersed during that season (-0.2 to $-2 \text{ W}\cdot\text{m}^{-2}$).
373 Distribution of anomalies of sulfate aerosols at 850 hPa (Figs. S2 a-d) and Figs. 4 a-d show
374 that in the Ind48 simulations, during all seasons, sulfate aerosols are transported south-west
375 over the Arabian Sea and partially to the east (during pre-monsoon, monsoon, and winter
376 towards Myanmar; during post-monsoon and winter to North-east China). These regions are
377 associated with negative radiative forcing for Ind48 in Figs. 6 a-d. This negative radiative
378 forcing extending from North India towards the Arctic during pre-monsoon and summer-
379 monsoon is likely due to the poleward transport of south Asian sulfate aerosols in the UTLS (2
380 $- 10 \mu\text{g}\cdot\text{m}^{-3}$) reflecting back solar radiation (see Figs. 4a, c). The poleward extension of
381 negative RF is not evident during the post-monsoon and winter seasons (Figs. 6 c, d). This
382 may be due to fine and thinner sulfate aerosol layer ($\sim 1 - 4 \mu\text{g}\cdot\text{m}^{-3}$) in the upper troposphere
383 which partially reflect back solar radiation, leading to weak positive and negative RF (-0.1 to
384 $+0.5 \text{ W}\cdot\text{m}^{-2}$) over mid-high latitudes ($40 - 70^\circ\text{N}$).

385 The simulated RF at TOA in the Ind48Chin70 simulations is negative over India
386 during all seasons (~ -0.6 to $-2 \text{ W}\cdot\text{m}^{-2}$) (Figs. 6e-h) similar to Ind48 (Figs. 6a-d). In addition,
387 the Chinese SO_2 emission reductions in Ind48Chin70 have produced a significant positive
388 forcing ~ 0.6 to $6 \text{ W}\cdot\text{m}^{-2}$ over China ($100 - 140^\circ\text{E}$). The positive RF is also seen over the
389 western Pacific (pre-monsoon, summer-monsoon, and winter) and Bay of Bengal (post-
390 monsoon and winter). This is due to the negative anomalies of sulfate aerosols over these
391 regions in Ind48Chin70 (Figs. S2 e-h). The south-west ward transport of Indian sulfate
392 aerosols to the Arabian Sea in the lower troposphere (Figs. S2 e-h) during all seasons
393 producing a negative RF in that region is evident in Figs. 6.e-h. During the monsoon season,
394 the narrow localized plume leads to a negative regional forcing ($30 - 40^\circ\text{N}$, $80 - 95^\circ\text{E}$) of \sim

395 0.6 $\text{W}\cdot\text{m}^{-2}$. The negative RF near 40 – 50 °N may be due to sulfate aerosols in the lower
396 troposphere (Fig. 5c). The negative RF values (-0.1 to $-0.4 \text{ W}\cdot\text{m}^{-2}$) extending from the Indian
397 region to the Arctic are likely due to the poleward transport in the upper troposphere during
398 the pre-monsoon season and in the lower-mid troposphere during the winter season (Figs. 6 e,
399 h). The seasonal mean net radiative forcing due to sulfate aerosols at the surface and at TOA
400 are similar for both the Ind48 and Ind48Chin70 simulations (Figs. S3 a-h), due to the strong
401 scattering properties of the sulfate aerosols (Forster et al., 2007).

402 The comparison of RF at the TOA obtained from ECHAM6–HAMMOZ simulations
403 over the Arabian Sea (60 – 75 °E, 0 – 20 °N) during winter (Ind48: $-2.0 \text{ W}\cdot\text{m}^{-2}$, Ind48Chin70:
404 $1.5 \text{ W}\cdot\text{m}^{-2}$) (Fig. 4a) show reasonable agreement with the INDOEX experiment (-1.25 to -2.0
405 $\text{W}\cdot\text{m}^{-2}$ over North India during January – March 1999 (Verma et al., 2012). Yu et al. (2016)
406 reported that the increase in sulfate AOD (0.06 – 0.15) over the tropics (30 °S – 30 °N) since
407 the pre-industrial period has exerted a forcing of -0.6 to $-1.3 \text{ W}\cdot\text{m}^{-2}$.

408 The corresponding distribution of sulfate aerosol DRF at TOA estimated with our
409 offline simulations for the four seasons for Ind48 and Ind48Chin70 are shown in Figs. 6 i-p.
410 The results from the offline model are in reasonable agreement with the ECHAM6–HAMMOZ
411 simulations, although their magnitude differs spatially. Both the Ind48 and Ind48Chin70
412 simulations have produced negative RFs, varying between -0.2 and $-2.0 \text{ W}\cdot\text{m}^{-2}$ over India. The
413 reduction of SO_2 emission over China leads to an increase in RF of 2 – $6 \text{ W}\cdot\text{m}^{-2}$, comparable
414 with the corresponding values simulated in ECHAM6–HAMMOZ. The differences in
415 estimated RF in the offline calculations and the ECHAM6–HAMMOZ simulations are likely
416 due to the fact that the implicit dynamical responses in ECHAM6–HAMMOZ are not captured

417 in the offline simulations. However, the offline calculations are important insofar as they
418 isolate the direct radiative impact of the simulated changes in aerosol loading.

419 The offline calculations further allow the specific effect of the enhanced aerosol layer
420 in the UTLS (300-50 hPa) to be discriminated (Figs. 7a-h). Figures 7a-d shows the direct
421 radiative forcing at TOA (estimated from our offline simulations) induced by the sulfate
422 aerosol enhancement in the UTLS (300 – 50 hPa) during the four seasons. The RF values from
423 Ind48 are mostly negative over India, China and extending to the Arctic (~ -0.001 to -0.015
424 $\text{W}\cdot\text{m}^{-2}$), due to the presence of the sulfate aerosol plume in the UTLS. Interestingly, the
425 Ind48Chin70 simulation also shows negative RFs in the region co-located with the UTLS
426 plume, e.g. in the summer-monsoon season, the plume over north India leads to negative RF
427 values. Similarly, in the post-monsoon season, the sulfate aerosols plume extends to 15S and
428 leads to negative RF values (~ -0.001 to $-0.005 \text{W}\cdot\text{m}^{-2}$) (see Fig 7g and Fig. S4). In the pre-
429 monsoon season, the aerosol plume travels to the Arctic below or near the tropopause,
430 therefore partial contribution to RF from the UTLS (300 to 50 hPa) might have produced
431 positive anomalies of 0.0001 to $0.0005 \text{W}\cdot\text{m}^{-2}$ in mid-high latitudes. During winter, sulfate
432 aerosols do not reach above the tropopause (Figs. 5 g-h) and therefore RF values are positive
433 over India and China. Thus the radiative forcing caused specifically by UTLS aerosol shows a
434 much clearer signal than the forcing due to the entire aerosol column (compare Figs. 6 and 7a-
435 h). The sulfate aerosol layer, corresponding to the ATAL in the summer monsoon season, in
436 the Ind48 simulation leads to a RF of ~ -0.011 to $-0.015 \text{W}\cdot\text{m}^{-2}$ (Fig.7b). It is reduced to -0.001
437 to $-0.003 \text{W}\cdot\text{m}^{-2}$ in the Ind48Chin70 simulations (Fig.7f) due to reduction of transport of
438 sulfate aerosols in the UTLS. The short term ATAL RF at TOA has previously been estimated
439 as about $\sim -0.1 \text{W}\cdot\text{m}^{-2}$ over the Asian region during 1998 – 2015 (Vernier et al., 2015). The

440 radiative forcing reported here caused solely by the sulfate aerosol particles in the UTLS is
441 lower than the value reported by Vernier et al. (2015), who give an integral value for the
442 ATAL and not only for the sulfate particles.

443 **5.2 Incoming solar radiation, temperature, and stability of the troposphere**

444 An important impact of sulfate aerosols in the atmosphere is solar dimming, which
445 counteracts the surface temperature response to the anthropogenic CO₂ increase (Ramanathan
446 et al., 2005). There is observational evidence (1300 sites globally) indicating that one-third of
447 potential continental warming attributable to increased greenhouse gas concentrations has
448 been compensated by aerosol cooling during 1964 – 2010 (Storelvmo et al., 2016). Solar
449 radiation measurements over the Indian region (at 12 stations) during 1981 – 2004 show a
450 declining trend varying between -0.17 to -1.44 W·m⁻² yr⁻¹ (Padma Kumari et al., 2007). While
451 not directly comparable to these previous studies, Ramanathan et al. (2005) reported a
452 negative trend in solar flux observations at 10 different Indian stations (-0.42 W·m⁻²) and their
453 model simulations show a trend of -0.37 W·m⁻² induced by the changes in BC and sulfate
454 aerosols over India (0 – 30 °N and 60 – 100 °E).

455 We estimate the changes in net solar radiation at the surface for four seasons from the
456 Ind48 and Ind48Chin70 simulations. Figures 7i-l shows that the Ind48 simulations have
457 produced negative anomalies in net solar radiation (SR) at the surface (~-0.5 to -3 W·m⁻²) over
458 India and parts of China (where sulfate aerosols are transported) due to the enhanced sulfate
459 aerosol layer reflecting back solar radiation. In general, the seasonal mean distribution of
460 anomalies in net solar radiation at the surface is similar to the distribution of the anomalies in
461 RF at the TOA. Reduction of Chinese SO₂ emissions along with an increase of SO₂ emissions

462 over India (Ind48Chin70) has produced a reduction of solar radiation over India while there is
463 a significant increase over China ($1 - 5 \text{ W}\cdot\text{m}^{-2}$) (see Figs. 7 m-p).

464 Sulfate aerosols also absorb infrared radiation thus causing heating locally and
465 producing a cooling in the region below by solar dimming (Niemeier and Schmidt, 2017).
466 Therefore, seasonally varying transport of sulfate aerosol may affect the thermal structure in
467 the receptor region. Figure 8 shows a temperature enhancement near the region of transport of
468 sulfate aerosols in the UTLS and a cooling of the atmosphere below it. For example, in the
469 Ind48 simulations, positive temperature anomalies are seen near the sulfate aerosol layer
470 extending to the Arctic, with negative anomalies below the layer during all seasons (except
471 winter) (Figs. 8 a-h). Similarly, a warming $\sim 0.1 - 0.7 \text{ K}$ over India simulated in the
472 Ind48Chin70 simulations in pre-monsoon and post-monsoon (Figs. 8 i-j, m-n). During winter,
473 in the Ind48Chin70 simulation, poleward transport occurs from the Indian lower/mid-
474 troposphere to the lower stratosphere of mid-high latitudes. This region shows positive
475 anomalies of temperature ~ 0.2 to 1 K (see Figs. 8 o-p and Figs. 5 g-h).

476 As shown in Figure 8 the amplitude of the temperature anomalies in the UTLS varies
477 seasonally and regionally. In general, there is temperature enhancement in the UTLS over
478 North India and South China ($20 - 35^\circ \text{N}$, $75 - 130^\circ \text{E}$) of $\sim 0.2 \pm 0.15$ to $0.8 \pm 0.72 \text{ K}$ in Ind48
479 (all four season) and $\sim 0.1 \pm 0.08$ to $0.5 \pm 0.23 \text{ K}$ in Ind48Chin70 (pre-monsoon and post-
480 monsoon). After reaching the Arctic, these sulfate aerosols cause substantial warming in the
481 lower stratosphere i.e. $\sim 1 \pm 0.62$ to $1.6 \pm 1.07 \text{ K}$ in Ind48 during all seasons and 0.7 ± 0.60 to
482 $1.6 \pm 1.43 \text{ K}$ in Ind48Chin70 in pre-monsoon and winter seasons. Figure 8 also shows reduction
483 in temperature of -0.1 ± 0.05 to $-0.6 \pm 0.4 \text{ K}$ in the troposphere, below the warming,
484 corresponding to the UTLS sulfate aerosols layer.

485 The changes in the circulation are illustrated in Figs. 9a-h. It shows ascending winds in
486 the region of the sulfate aerosol plume. For example the Ind48 simulations show ascending
487 winds over northern India during all seasons and in the Ind48Chin70 simulations during the
488 pre-monsoon season. The reduction of Chinese SO₂ emissions (Ind48China70) induces strong
489 descending winds over northern India during the summer-monsoon and post-monsoon. It
490 hindered the poleward transport of the plume as discussed in section 4.2.

491 The sulfate aerosol-induced cooling in the upper troposphere (below the layer of
492 sulfate aerosols) and subsidence in the upper troposphere cause a stabilization of the upper
493 troposphere (Pitari et al., 2016). Figures 9 i-p shows that anomalies of Brunt-Väisälä
494 frequency are positive ($0.2 - 3 \text{ s}^{-1} \times 10^{-5}$) in the upper troposphere (250 – 150 hPa) over north
495 India and south China (20 – 35 °N, 70 – 130 °E) during all the seasons in Ind48 and for the
496 pre-monsoon and post-monsoon season in the Ind48Chin70 simulations. Thus enhanced Indian
497 sulfate aerosols have increased the stability of the upper troposphere and produce a cooling of
498 ~0.2 – 1.2K (Fig.8) in the upper troposphere. They have induced upper tropospheric
499 subsidence (10 – 30 °N) in Ind48 and ind48Chin70 simulations (except in winter in
500 Ind48Chin70). Upper tropospheric temperature and stability play important roles in rainfall
501 suppression (Wu and Zhang, 1998; Fadnavis and Chattopadhyay, 2017). Thus [upper](#)
502 [tropospheric cooling and enhanced stability may suppress the rainfall](#) in all seasons in Ind48
503 and in the pre-monsoon and post-monsoon season in the Ind48Chin70 simulations. However, a
504 complete analysis of the impact of the enhanced surface aerosols on rainfall is beyond the
505 scope of this study.

506

507 5.3 Cirrus Clouds

508 Cirrus clouds cover at least about 30 % of the Earth's area on annual average (Stubenrauch
509 et al., 2013, Gasparini et al., 2018), occurring mainly between 400 – 100 hPa altitude. They play
510 an important role in the Earth's energy budget (Gasparini and Lohmann, 2016; Hartmann et al.,
511 2018), in transport of water vapor into the stratosphere (Randel and Jensen, 2013), as well as in
512 the atmospheric heat and energy cycle (Crueger and Stevens, 2015). Cirrus clouds can form by
513 either homogeneous nucleation by freezing of dilute sulfate aerosols or by heterogeneous ice
514 nucleation in the presence of ice nuclei, most commonly dust (Ickes et al., 2015; Cziczo et al.,
515 2017). Moreover, a large fraction of cirrus clouds have a [liquid origin](#) as the ice crystals were
516 either nucleated at mixed-phase conditions and transported to lower temperatures or detrained
517 from convective cloud tops (Krämer et al., 2016; Wernli et al., 2016; Gasparini et al., 2018). All
518 mentioned formation processes except heterogeneous nucleation of ice crystals below the
519 homogeneous freezing temperature (i.e. at cirrus conditions) are represented in by our model
520 simulations. However, heterogeneous freezing on dust and black carbon aerosols is included in
521 mixed-phase clouds (Lohmann and Hoose, 2009), for temperatures between freezing and -35°C .
522 [Figures 10 a-h shows the impact of SO₂ emission changes on cirrus clouds. It shows a decrease](#)
523 [\(5 – 30 %\) of cirrus clouds over North India \(20 – 35 °N\) in the UTLS.](#) The decrease in cirrus
524 clouds coincides with is a significant decrease of ice crystal number concentration by -0.15 to $-$
525 0.5 cm^{-3} between 250 – 50 hPa (except in winter in Ind48Chin70 since the plume of sulfate
526 aerosols does not reach the upper troposphere) (Figs. 10i–p).

527 Our analysis indicates that an increase in the upper tropospheric sulfate aerosol
528 concentration leads to a temperature increase in the upper troposphere and lower stratosphere
529 of about $\sim 0.2 \pm 0.15$ to 0.8 ± 0.72 K over north India and South China and to a cooling below

530 (Fig. 8). This temperature increase causes a decrease in the upper tropospheric temperature
531 gradient and vertical velocity, concurrently an increase in the upper tropospheric (200 – 100
532 hPa) static stability (Brunt–Väisälä frequency) (over 80 – 120 °E) (Figs. 9 i-p) (Figs. 9 a-h). A
533 combination of decreased upper tropospheric updraft motion and increased temperature
534 decreases the likelihood of cirrus cloud formation in a similar way as for the simulated
535 responses to volcanic eruptions or stratospheric sulfur geoengineering (Kuebbeler et al., 2012,
536 Pitari et al. 2016, Visioni et al., 2018a).

537

538 **6. Discussion**

539 Our model simulations presented here provide seasonal transport processes and
540 estimates of radiative forcing for the year 2011. The inter-annual variability in the transport
541 processes may impact the injection of sulfate aerosols shallow/deep into the lower
542 stratosphere. The stratospheric warming produced in response to the transport of rising South
543 Asian anthropogenic sulfate aerosol in the UTLS over Asia and further to the Arctic (Fig. 4
544 and Fig.5) may modulate the Quasi-biennial Oscillation (QBO) and thereby the transport of
545 sulfate aerosol from the tropics to the extra-tropics. The QBO phases are modulated by the
546 amount of sulfate and height of the injection (Aquila et al., 2014; Niemeier and Schmidt,
547 2017; Visioni et al., 2018b). A previous study reports that the QBO slows down after an
548 injection of 4 Tg (S) yr⁻¹ into the stratosphere and completely shuts it down after the injection
549 of 8 Tg (S) yr⁻¹ (Niemeier and Schmidt, 2017). However, another model study finds that the
550 QBO, even for larger amount of SO₂ injections, does not deviate much from present day
551 conditions (Richter et al., 2018). These studies indicate that there is a complicated interaction
552 between UTLS aerosols, atmospheric dynamics and atmospheric chemistry (Richter et al.,

553 2017; Niemeier and Schmidt, 2017; Vioni et al., 2018b). The QBO is known to modulate the
554 tropical convection (Collimore et al., 2003; Fadnavis et al., 2013; Nie and Sobel, 2015). Thus
555 transport of sulfate aerosols into the stratosphere would impact the tropospheric hydrological
556 cycle in addition to the tropospheric aerosol loading. The increasing amounts of tropospheric
557 sulfate aerosol loading are linked with droughts via changes in radiative forcing, stability, and
558 tropospheric temperature gradient (Yeh et al., 2015; Kim et al., 2016). Simulations for a longer
559 time period and with the inclusion of QBO phases may reveal the influence of current SO₂
560 emission on tropospheric-stratospheric dynamics and the hydrological cycle. Nonetheless, the
561 results of the current study show the impacts of sulfate aerosols on the UTLS for realistic
562 emission perturbations over India and China.

563

564 **7. Conclusions**

565 This study investigated the long range transport of Asian sulfate aerosols and their
566 associated impacts on radiative forcing, temperature, circulation and cirrus clouds using
567 ECHAM6–HAMMOZ model simulations. We considered emissions perturbations of
568 anthropogenic SO₂ derived from OMI observations, namely (1) enhancement over India by 48
569 % (Ind48) and (2) enhancement over India by 48% and reduction over China by 70 %
570 simultaneously (Ind48Chin70). Ind48 simulations show long-range transport of sulfate
571 aerosols from the Indian boundary layer (75 – 95 °E, 20 – 35 °N) to the UTLS and further
572 horizontally to the Arctic throughout the year. The reduction of Chinese SO₂ emissions inhibits
573 the transport of sulfate aerosols from India to the Arctic in the summer-monsoon and post-
574 monsoon seasons via subsidence over north India, which is induced in response to emission
575 perturbation. The enhancement of Indian emission increases the aerosol burden (AOD) in the

576 UTLS over North India by 0.184E-04 (1.1 %) to 19.20E-04 (19.25 %) and Arctic by 0.17E-04
577 (3.3 %) to 2.09E-04 (16.45 %). This leads to a warming ($\sim 0.2 \pm 0.15$ to 0.8 ± 0.72 K) in the
578 UTLS near the sulfate aerosol layer and to a cooling below it in the troposphere (0.1 ± 0.05 to -
579 0.6 ± 0.4 K). It produces a negative net radiative forcing at TOA -0.2 to $-2 \text{ W}\cdot\text{m}^{-2}$ over North
580 India. There is a substantial increase of ~ 0.6 to $6 \text{ W}\cdot\text{m}^{-2}$ in net radiative forcing at TOA over
581 China in response to the reduction of Chinese SO_2 emissions.

582 The RF at the TOA estimated from the offline radiative transfer model for
583 enhancement of Indian SO_2 emission is -0.2 to $-2.0 \text{ W}\cdot\text{m}^{-2}$ over India. The reduction of SO_2
584 emissions over China leads to an RF of 2 to $6 \text{ W}\cdot\text{m}^{-2}$. These values are comparable with
585 results of the ECHAM6–HAMMOZ simulations, with the minor differences likely due to the
586 implicit dynamical impacts in response to enhanced south Asian SO_2 emissions in ECHAM6–
587 HAMMOZ not being represented in the offline model. The enhancement of sulfate aerosols in
588 the UTLS (300 – 50 hPa) produces a negative forcing in the region co-located with sulfate
589 aerosol layer in the UTLS, extending from India to the Arctic in the Ind48 (-0.003 to -0.015
590 $\text{W}\cdot\text{m}^{-2}$) and the Ind48Chin70 (-0.001 – $-0.005 \text{ W}\cdot\text{m}^{-2}$) simulations. The ATAL in the Ind48
591 simulation has produced an RF over north India of ~ -0.011 – $0.015 \text{ W}\cdot\text{m}^{-2}$ (Fig.7b), which has
592 reduced to -0.001 – $-0.003 \text{ W}\cdot\text{m}^{-2}$ in the Ind48Chin70 simulation (Fig.7f). This reduction is
593 attributed to the subsidence over north India produced by the Chinese SO_2 emission reduction..

594 An enhancement of 48 % in South Asian anthropogenic sulfate aerosols leads to a decrease in
595 cirrus clouds, cooling of the mid-upper troposphere over the northern regions of India and
596 south China throughout the year. This enhances the stability (anomalies in Brunt Väisälä
597 frequency 0.2 to $2 \text{ s}^{-1} \times 10^{-5}$) of the upper troposphere (~ 250 hPa) of these regions. Reduction
598 of Chinese SO_2 emissions does not stabilize the upper troposphere during monsoon and winter

599 seasons since subsidence over North India is inhibited the vertical transport of sulfate aerosols
600 to the UTLS. Upper tropospheric temperature and stability play an important role in rainfall
601 reduction. Strong subsidence, mid-upper tropospheric cooling and enhanced stability are the
602 features associated with rainfall deficit (Wu and Zhang, 1998; Fadnavis et al., 2017c). The link
603 between these features and rainfall deficit should be addressed in future research. It is
604 important to note that an increase in surface emissions of SO₂ does not necessarily lead to a
605 reduction in RF (as might be expected) but that regional enhancements of RF might occur in
606 response to an inherent dynamical response (including changes in high cloud cover) to
607 enhanced SO₂ emissions.

608

609 Data availability: OMI SO₂ data can be obtained from
610 https://disc.gsfc.nasa.gov/datasets/OMSO2e_V003/summary?keywords=aura, MISR data is
611 available at <https://giovanni.gsfc.nasa.gov/giovanni/>, CALIPSO, and CloudSat measurements
612 can be obtained from <http://www.cloudsat.cira.colostate.edu/data-products/>. These satellite
613 data sets are freely available.

614 Author contributions: S.F. designed the study and wrote the paper, G.K. analyzed the model
615 simulations, M.R and A.R. performed offline radiative forcing computations. J.-Li provided
616 CALIPSO data. B.G and A.L. helped with aerosols and cirrus cloud analysis. R.M. contributed
617 to the analysis of the model results and the writing of the manuscript.

618 *Acknowledgments:* Suvarna Fadnavis acknowledges Prof. Ravi Nanjundiah, Director of IITM,
619 with gratitude for his encouragement during this study. The [authors thank the anonymous](#)
620 [reviewers for valuable suggestions](#) and the high-performance computing team at IITM for
621 supporting the model simulations.

622

623

624

625

626 **References:**

627

628 Aas, W., Mortier, A., Bowersox, V., Ribu, C., Faluvegi, G., Fagerli, H., Hand, J., Klimont, Z.,

629 Galy-Lacaux, C., Lehmann, C. M. B., Myhre, C. L., Myhre, G., Olivié, D., Sato, K.,

630 Quaas, J., Rao, P. S. P., Schulz, M., Shindell, D., Skeie, R. B., Stein, A., Takemura, T.,

631 Tsyro, S., Robert, Vet R., and Xiaobin Xu, X.: Global and regional trends of atmospheric

632 sulfur, *Sci. Reports*, 9, 953, <https://doi.org/10.1038/s41598-018-37304-0>, 2019.

633 Aquila, V., Garfinkel, C. I., Newman, P. A., Oman, L. D., and Waugh, D. W.: Modifications

634 of the quasi-biennial oscillation by a geoengineering perturbation of the stratospheric

635 aerosol layer, *Geophys. Res. Lett.*, 41, 1738–1744,

636 <https://doi.org/10.1002/2013GL058818>, 2014.

637 Babu, S. S., Manoj, M. R., Moorthy, K. K., Gogoi, M. M., Nair, V. S., Kompalli, S. K.,

638 Satheesh, S. K., Niranjana, K., Ramagopal, K., Bhuyan, P. K., and Singh, D.: Trends in

639 aerosol optical depth over Indian region: Potential causes and impact indicators, *J.*

640 *Geophys. Res.*, 118, 11,794–11,806, doi:10.1002/2013JD020507, 2013.

641 Bellouin, N., Rae, J., Jones, A., Johnson, C., Haywood, J., and Boucher, O.: Aerosol forcing

642 in the Climate Model Intercomparison Project (CMIP5) simulations by HadGEM2-ES

643 and the role of ammonium nitrate, *J. Geophys. Res.*, 116, D20206,

644 doi:10.1029/2011JD016074, 2011.

645 Bourgeois, Q. and Bey, I.: Pollution transport efficiency toward the Arctic: Sensitivity to

646 aerosol scavenging and source regions, *J. Geophys. Res.*, 116, D08213,

647 doi:10.1029/2010JD015096, 2011.

648 Collimore, C. C., Martin, D. W., Hitchman, M. H., Huesmann, A., and Waliser, D. E.: On
649 the relationship between the QBO and tropical deep convection, *J. Clim.*, 16, 2552 –
650 2568, [https://doi.org/10.1175/1520-0442\(2003\)016<2552:OTRBTQ>2.0.CO;2](https://doi.org/10.1175/1520-0442(2003)016<2552:OTRBTQ>2.0.CO;2), 2003.

651 Crueger, T. and Stevens, B.: The effect of atmospheric radiative heating by clouds on the
652 Madden-Julian Oscillation, *J. Adv. Model. Earth Syst.*, 7, 854–864,
653 [doi:10.1002/2015MS000434](https://doi.org/10.1002/2015MS000434), 2015.

654 Cziczo, D. J., Ladino, L., Boose, Y., Kanji, Z. A., Kupiszewski, P., Lance, S., Mertes, S., and
655 Wex, H.: Measurements of ice nucleating particles and ice residuals, *Meteorological*
656 *Monographs*, 58, 8.1-8.13. <https://doi.org/10.1175/AMSMONOGRAPHS-D-16-0008.1>,
657 2017.

658 Deng, M., Mace, G. G., Wang, Z., and Lawson, R. P.: Evaluation of Several A-Train Ice
659 cloud retrieval products with in situ measurements collected during the SPARTICUS
660 campaign, *J. Appl. Meteorol. Clim.*, 52, 1014–1030, [https://doi.org/10.1175/JAMCD-12-](https://doi.org/10.1175/JAMCD-12-054.1)
661 [054.1](https://doi.org/10.1175/JAMCD-12-054.1), 2013.

662 Dumka, U. C., Tripathi, S. N., Misra, A., Giles, D. M., Eck, T. F., Sagar, R., and Holben, B.
663 N.: Latitudinal variation of aerosol properties from Indo-Gangetic Plain to central
664 Himalayan foothills during TIGERZ campaign, *J. Geophys. Res.*, 119, 4750–4769,
665 [doi:10.1002/2013JD021040](https://doi.org/10.1002/2013JD021040), 2014.

666 Edwards, J. M. and Slingo, A.: Studies with a Flexible New Radiation Code. I: Choosing a
667 Configuration for a Large-Scale Model, *Quart. J. Roy. Meteorol. Soc.*, 122, 689-719,
668 <http://dx.doi.org/10.1002/qj.49712253107>, 1996.

669 Fadnavis, S., Roy, C., Chattopadhyay, R., Sioris, C. E., Rap, A., Müller, R., Kumar, R. K., and
670 Krishnan, R.: Transport of trace gases via eddy shedding from the Asian summer

671 monsoon anticyclone and associated impacts on ozone heating rates, *Atmos. Chem. Phys.*,
672 18, 11493–11506, <https://doi.org/10.5194/acp-18-11493-2018>, 2018.

673 Fadnavis, S., Kalita, G., Kumar, K. R., Gasparini, B., and Li, J. L.: Potential impact of
674 carbonaceous aerosol on the upper troposphere and lower stratosphere (UTLS) and
675 precipitation during Asian summer monsoon in a global model simulation, *Atmos. Chem.*
676 *Phys.*, 17, 11637-11654, <https://doi.org/10.5194/acp-17-11637-2017>, 2017a.

677 Fadnavis, S., Roy, C., Sabin, T. P., Ayantika, D. C., and Ashok, K.: Potential modulations of
678 pre-monsoon aerosols during El Niño: impact on Indian summer monsoon, *Clim.*
679 *Dynam.*, 49, 2279–2290, <https://doi.org/10.1007/s00382-016-3451-6>, 2017b.

680 Fadnavis, S. and Chattopadhyay, R.: Linkages of subtropical stratospheric intraseasonal
681 intrusions with Indian summer monsoon deficit rainfall, *J. Clim.*, 30, 5083–5095,
682 <https://doi.org/10.1175/JCLI-D-16-0463.1>, 2017.

683 Fadnavis, S., Semeniuk, K., Pozzoli, L., Schultz, M. G., Ghude, S. D., Das, S., and Kakatkar,
684 R.: Transport of aerosols into the UTLS and their impact on the Asian monsoon region as
685 seen in a global model simulation, *Atmos. Chem. Phys.*, 13, 8771–8786,
686 <https://doi.org/10.5194/acp-13-8771-2013>, 2013.

687 Fadnavis, S. and Beig, G.: Seasonal variation of trend in temperature and ozone over the
688 tropical stratosphere in the Northern Hemisphere, *J. Atmos. Solar Terrestrial Phys.*, 68,
689 1952-1961, doi: 10.1016/j.jastp.2006.09.003, 2006.

690 Fisher, J. A., Jacob, D. J., Wang, Q., Bahreini, R., Carouge, C. C., Cubison, M. J., Dibb, J.E.,
691 Diehl, T., Jimenez, J. L., Leibensperger, E. M., Lu, Z., Meinders, M. B. J., Pye, H. O. T.,
692 Quinn, P. K., Sharma, S., Streets, D. G., Donkelaar, A. van, and Yantosca, R. M.:
693 Sources, distribution, and acidity of sulfate-ammonium aerosol in the Arctic in winter-

694 spring, *Atmospheric Environment*, 45, 7301-7318, DOI: 10.1016/j.atmosenv.2011.08.030,
695 2011.

696 Forster, P., Ramaswamy, V., Artaxo, P., Berntsen, T., Betts, R., Fahey, D. W., Haywood, J.,
697 Lean, J., Lowe, D. C., Myhre, G., Nganga, J., Prinn, R., Raga, G., Schulz M., and R. Van
698 Dorland, 2007: Changes in Atmospheric Constituents and in Radiative Forcing. In:
699 *Climate Change 2007: The Physical Science Basis. Contribution of Working Group I to*
700 *the Fourth Assessment Report of the Intergovernmental Panel on Climate Change*
701 [Solomon, S., D. Qin, M. Manning, Z. Chen, M. Marquis, K.B. Averyt, M.Tignor and
702 H.L. Miller (eds.)], Cambridge University Press, Cambridge, United Kingdom and New
703 York, NY, USA, 129-234, 2007.

704 Gasparini, B., Meyer, A., Neubauer, D., Münch, S., and Lohmann, U.: Cirrus Cloud Properties
705 as Seen by the CALIPSO Satellite and ECHAM–HAM Global Climate Model, *J. Clim.*,
706 31, 1983–2003, <https://doi.org/10.1175/JCLI-D-16-0608.1>, 2018.

707 Gasparini, B., and Lohmann, U.: Why cirrus cloud seeding cannot substantially cool the
708 planet, *J. Geophys. Res.*, 121, 4877–4893, <https://doi.org/10.1002/2015JD024666>, 2016.

709 Gu, Y., Liao, H., and Bian, J.: Summertime nitrate aerosol in the upper troposphere and lower
710 stratosphere over the Tibetan Plateau and the South Asian summer monsoon region,
711 *Atmos. Chem. Phys.*, 16, 6641-6663, <https://doi.org/10.5194/acp-16-6641-2016>, 2016.

712 Hartmann, D. L., Gasparini, B., Berry, S. E., and Blossey, P. N.: The Life Cycle and Net
713 Radiative Effect of Tropical Anvil Clouds, *Journal of Advances in Modeling Earth*
714 *Systems*, 10, 3012–3029, <https://doi.org/10.1029/2018MS001484>, 2018.

715 Holben, B. N., Eck, T. F., Slutsker, I., Tanré, D., Buis, J. P., Setzer, A., Vermote, E., Reagan,
716 J. A., Kaufman, Y. J., Nakajima, T., Lavenu, F., Jankowiak, I., and Smirnov, A.:

717 AERONET: Federated Instrument Network and Data Archive for Aerosol
718 Characterization, *Remote Sens. Environ.*, 66, 1–16, [https://doi.org/10.1016/S0034-](https://doi.org/10.1016/S0034-4257(98)00031-5)
719 4257(98)00031-5, 1998.

720 Höpfner, M., J. Ungermann, S. Borrmann, R. Wagner, R. Spang, M. Riese, G. Stiller, et al.:
721 Ammonium nitrate particles formed in upper troposphere from ground ammonia sources
722 during Asian monsoons, *Nat. Geosci.*, in press, 2019.

723 Ickes, L., Welti, A., Hoose, C., and Lohmann, U.: Classical nucleation theory of homogeneous
724 freezing of water: thermodynamic and kinetic parameters, *Phys. Chem. Chem. Phys.*, 17,
725 5514–5537, [10.1039/C4CP04184D](https://doi.org/10.1039/C4CP04184D), 2015.

726 Kahn, R., Banerjee, P. D., McDonald, D.: The sensitivity of multiangle imaging to natural
727 mixtures of aerosols over ocean, *J. Geophys. Res.*, 106, 18219–18238,
728 <https://doi.org/10.1029/2000JD900497>, 2001.

729 Kim, M. J., Yeh, S. W., and Park, R. J.: Effects of sulfate aerosol forcing on East Asian
730 summer monsoon for 1985–2010, *Geophys. Res. Lett.*, 43, 1364–1372,
731 [doi:10.1002/2015GL067124](https://doi.org/10.1002/2015GL067124), 2016.

732 Kinnison, D. E., Brasseur, G. P., Walters, S., et al.: Sensitivity of chemical tracers to
733 meteorological parameters in the MOZART-3 chemical transport model, *J. Geophys.*
734 *Res.*, 112,D20302, 1–24, <https://doi.org/10.1029/2006JD007879>, 2007.

735 Kokkola, H., Kühn, T., Laakso, A., et al.: SALSA2.0: The sectional aerosol module of the
736 aerosol–chemistry–climate model ECHAM6.3.0-HAM2.3-MOZ1.0, *Geosci. Model Dev.*,
737 11, 3833–3863, <https://doi.org/10.5194/gmd-11-3833-2018>, 2018.

738 Krämer M., Rolf, C., Luebke A., Afchine, A., et al.: A microphysics guide to cirrus clouds,
739 *Atmos. Chem. Phys.*, 16, 3463–3483, <https://doi.org/10.5194/acp-16-3463-2016>, 2016.

740 Kremser, S., Thomason, L. W., von Hobe, M., et al: Stratospheric aerosol-Observations,
741 processes and impact on climate, *Rev. Geophys.*, 54, 278–335,
742 <https://doi.org/10.1002/2015RG000511>, 2016.

743 Krotkov, N. A., McLinden, C. A., Li, C., et al.: Aura OMI observations of regional SO₂ and
744 NO₂ pollution changes from 2005 to 2015, *Atmos. Chem. Phys.*, 16, 4605–4629.
745 <https://doi.org/10.5194/acp-16-4605-2016>, 2016.

746 Kuebbeler, M., Lohmann, U., and Feichter, J.: Effects of stratospheric sulfate aerosol geo-
747 engineering on cirrus clouds, *Geophys. Res. Lett.*, 39, L23803, 1–5.
748 <https://doi.org/10.1029/2012GL053797>, 2012.

749 Lau, W. K. M., Yuan, C., and Li, Z.: Origin, Maintenance and Variability of the Asian
750 Tropopause Aerosol Layer (ATAL): The Roles of Monsoon Dynamics, *Sci. Rep.*, 8,
751 3960, 1–14. <https://doi.org/10.1038/s41598-018-22267-z>, 2018.

752 Lelieveld, J., Bourtsoukidis, E., Brühl, C., Fischer, H., Fuchs, H., Harder, H., Hofzumahaus,
753 A., Holland, F., Marno, D., Neumaier, M., Pozzer, A., Schlager H., Williams, J., Zahn,
754 A., and Ziereis, H.: The South Asian monsoon pollution pump and purifier, *Science*, 361,
755 270–273, <https://doi.org/10.1126/science.aar2501>, 2018.

756 Levelt, P. F., et al.: The Ozone Monitoring Instrument, *IEEE Trans. Geosci. Remote Sensing*,
757 44, 1093–1101, 2006.

758 Li, J.-L.F., Waliser, D. E., Chen, W. T., et al.: An observationally based evaluation of cloud
759 ice water in CMIP3 and CMIP5 GCMs and contemporary reanalyses using contemporary
760 satellite data, *J. Geophys. Res.*, 117, D16105, doi:10.1029/2012JD017640, 2012.

761 Li, C., McLinden, C., Fioletov, V., Krotkov, Carn, S., Joiner, J., Streets, D., He, H., Ren, X.,
762 Li, Z., and Dickerson, R. R.: India is overtaking China as the world’s largest emitter of

763 anthropogenic sulfur dioxide, *Sci. Rep.*, 7, 14304, DOI:10.1038/s41598-017-14639-8,
764 2017.

765 Lohmann, U. and Ferrachat, S.: Impact of parametric uncertainties on the present-day climate
766 and on the anthropogenic aerosol effect, *Atmos. Chem. Phys.*, 10, 11373-11383,
767 doi:10.5194/acp-10-11373-2010, 2010.

768 Lohmann, U. and Hoose, C.: Sensitivity studies of different aerosol indirect effects in mixed-
769 phase clouds, *Atmos. Chem. Phys.*, 9, 8917-8934, [https://doi.org/10.5194/acp-9-8917-](https://doi.org/10.5194/acp-9-8917-2009)
770 2009, 2009.

771 Luo, Y., Wang, H., Zhang, R., Qian, W., and Luo, Z.: Comparison of Rainfall Characteristics
772 and Convective Properties of Monsoon Precipitation Systems over South China and the
773 Yangtze and Huai River Basin, *J. Clim.*, 26, 110-132 DOI: 10.1175/JCLI-D-12-00100.1,
774 <https://doi.org/10.1175/JCLI-D-12-00100.1>, 2013.

775 Manohar, G. K., Kahdalgaonkar, S. S., and Tinmaker, M. I. R.: Thunderstorm activity over
776 India and the Indian southwest monsoon, *J. Geophys. Res.*, 104, 4169–4188,
777 <https://doi.org/10.1029/98JD02592>, 1999.

778 Martonchik, J. V, Diner, D. J., Crean, K. A., and Bull, M. A.: Regional aerosol retrieval results
779 from MISR, *IEEE Trans. Geosci. Remote Sens.*, 40, 1520–1531, 2002.

780 Medina, S., Houze Jr., R. A., Kumar, A., Niyogi, D.: Summer monsoon convection in the
781 Himalayan region: Terrain and land cover effects, *Quart. J. Roy. Meteorol. Soc.*, 136, 593
782 – 616, DOI: 10.1002/qj.601, 2010.

783 Myhre, G., Shindell, D., Bréon, F.-M., et al.: Anthropogenic and Natural Radiative Forcing.
784 *Climate Change 2013: The Physical Science Basis. Contribution of Working Group I to*

785 the Fifth Assessment Report of the Intergovernmental Panel on Climate Change, 659–
786 740, <https://doi.org/10.1017/CBO9781107415324.018>, 2013.

787 Neubauer, D., Lohmann, U., Hoose, C., and Frontoso, M. G.: Impact of the representation of
788 marine stratocumulus clouds on the anthropogenic aerosol effect, *Atmos. Chem. Phys.*,
789 14, 11997–12022, doi:10.5194/acp-14-11997-2014, 2014.

790 Nie, J. and Sobel, A. H.: Responses of Tropical Deep Convection to the QBO: Cloud-
791 Resolving Simulations, *J. Atmos., Sci.*, 72, 3625-3638, DOI: 10.1175/JAS-D-15-0035.1,
792 2015.

793 Niemeier, U. and Schmidt, H.: Changing transport processes in the stratosphere by radiative
794 heating of sulfate aerosols, *Atmos. Chem. Phys.*, 17, 14871–14886.
795 <https://doi.org/10.5194/acp-17-14871-2017>, 2017.

796 Padma Kumari, B., Londhe, A. L., Daniel, S., and Jadhav, D. B.: Observational evidence of
797 solar dimming: Offsetting surface warming over India, *Geophys. Res. Lett.*, 34, L21810,
798 1–5. <https://doi.org/10.1029/2007GL031133>, 2007.

799 Paul, S., Ghosh, S., Oglesby, R., Pathak, A., Chandrasekharan, A., and Ramsankaran, R.:
800 Weakening of Indian Summer Monsoon Rainfall due to Changes in Land Use Land
801 Cover, *Sci. Rep.*, 6, 32177, 1–10, <https://doi.org/10.1038/srep32177>, 2016.

802 Pitari, G., Visionsi, D., Mancini, E., Cionni, I., Genova, G. Di., and Gandilfi, I.: Sulfate
803 aerosols from non-explosive volcanoes: chemical radiative effects in the troposphere and
804 lower stratosphere, *Atmosphere*, 7, 85, doi:10.3390/atmos7070085, 2016.

805 Pu, B. and Ginoux, P.: How reliable are CMIP5 models in simulating dust optical depth?,
806 *Atmos. Chem. Phys.*, 18, 12491-12510, <https://doi.org/10.5194/acp-18-12491-2018>, 2018.

807 Ramanathan, V., Chung, C., Kim, D., Bettge, T., Buja, L., Kiehl, J. T., Washington, W. M.,
808 Fu, Q., Sikka, D. R., and Wild, M.: Atmospheric brown clouds: Impacts on South Asian
809 climate and hydrological cycle, *P. Natl. Acad. Sci.*, 102, 5326–5333.
810 <https://doi.org/10.1073/pnas.0500656102>, 2005.

811 Randel, W. and Jensen, E.: Physical processes in the tropical tropopause layer and their role in
812 a changing climate, *Nat. Geosci.*, 6, 169–176, <https://doi.org/10.1038/ngeo1733>, 2013.

813 Rap, A., Scott, C. E., Spracklen, D.V., Bellouin, N., Forster, P. M., Carslaw, K. S., Schmidt,
814 A. and Mann, G.: Natural aerosol direct and indirect radiative effects, *Geophys. Res.*
815 *Lett.*, 40, 3297–3301, doi:10.1002/grl.50441, 2013.

816 Richter, J. H., Tilmes, S., Glanville, A., Kravitz, B., MacMartin, D. G., Mills, M. J., Simpson,
817 I. R., Vitt, F., Tribbia, J. J., and Jean-Francois, L.: Stratospheric response in the first
818 geoengineering simulation meeting multiple surface climate objectives, *J. Geophys. Res.*,
819 123, 5762–5782, <https://doi.org/10.1029/2018JD028285>, 2018.

820 Richter, J. H., Tilmes, S., Mills, M. J., Tribbia, J. J., Kravitz, B., MacMartin, D. G., Vitt, F.,
821 Jean-Francois, L.: Stratospheric dynamical response and ozone feedbacks in the presence
822 of SO₂ injections, *J. Geophys. Res.*, 122, 12,557–12,573,
823 <https://doi.org/10.1002/2017JD026912>, 2017.

824 Shawki, D., Voulgarakis, A., Chakraborty, A., Kasoar, M., and Srinivasan, J.: The South
825 Asian monsoon response to remote aerosols: Global and regional mechanisms. *J.*
826 *Geophys. Res.*, 123, 11,585–11,601. <https://doi.org/10.1029/2018JD028623>, 2018.

827 Shindell, D. T., Chin, M., Dentener, F., et al.: A multi-model assessment of pollution transport
828 to the Arctic, *Atmos. Chem. Phys.*, 8, 5353–5372, [https://doi.org/10.5194/acp-8-5353-](https://doi.org/10.5194/acp-8-5353-2008)
829 2008.

830 Spada, M., Jorba, O., Pérez García-Pando, C., Janjic, Z, Baldasano, J. M.: Modeling and
831 evaluation of the global sea-salt aerosol distribution: sensitivity to size-resolved and sea-
832 surface temperature dependent emission schemes, *Atmos. Chem. Phys.*, 13, 11735–
833 11755. doi:10.5194/acp-13-11735-2013, 2013.

834 SPARC-ASAP, Assessment of Stratospheric Aerosol Properties (ASAP), WCRP-124,
835 WMO/TD No. 1295, SPARC Rep. 4, 348 pp., 2006.

836 Stier, P., Feichter, J., Kinne, S., Kloster, S., Vignati, E., Wilson, J., et al.: The aerosol-climate
837 model ECHAM5-HAM, *Atmos. Chem. Phys.*, 5, 1125-1156, doi:10.5194/acp-5-1125-
838 2005, 2005.

839 Storelvmo, T., Leirvik, T., Lohmann, U., Phillips, P. C. B., and Wild, M.: Disentangling
840 greenhouse warming and aerosol cooling to reveal Earth's climate sensitivity, *Nat.*
841 *Geosci.*, 9, 286-289, <http://doi.org/10.1038/NGEO2670>, 2016.

842 Stubenrauch, C. J., Rossow, W. B., Kinne, S., Ackerman, S., Cesana, G., Chepfer, H., et al.:
843 Assessment of Global Cloud datasets from Satellites: Project and Database initiated by
844 the GEWEX Radiation Panel, *Bull. Amer. Meteor. Soc.*, 1031-1048.
845 <https://doi.org/10.1175/BAMS-D-12-00117.1>, 2013.

846 Taylor, K. E., Williamson, D., and Zwiers, F.: The sea surface temperature and sea-ice
847 concentration boundary conditions of AMIP II simulations, PCMDI Rep. 60, 20 pp, 2000.

848 Tegen, I., Neubauer, D., Ferrachat, S., Siegenthaler-Le Drian, C., et al.: The aerosol-climate
849 model ECHAM6.3-HAM2.3: Aerosol evaluation, *Geosci. Model Dev.*, 12, 1643–1677,
850 <https://doi.org/10.5194/gmd-12-1643-2019>, 2019.

851 Textor, C., Schulz, M., Guibert, S., Kinne, S., Balkanski, Y., Bauer, S., Bernsten, T., et al.:
852 Analysis and quantification of the diversities of aerosol life cycles within AeroCom,
853 Atmos. Chem. Phys., 6, 1777-1813, <https://doi.org/10.5194/acp-6-1777-2006>, 2006.

854 Verma, S., Boucher, O., Reddy, M. S., Upadhyaya, H. C., Van, P. Le, Binkowski, F. S. and
855 Sharma, O. P.: Tropospheric distribution of sulfate aerosols mass and number
856 concentration during INDOEX-IFP and its transport over the Indian Ocean: A GCM
857 study, Atmos. Chem. Phys., 12, 6185–6196. <https://doi.org/10.5194/acp-12-6185-2012>,
858 2012.

859 Vernier, J.-P., Fairlie, T. D., Deshler, T., Venkat Ratnam, M. et al.: BATAL: The balloon
860 measurement campaigns of the Asian tropopause aerosol layer, Bull. Amer. Meteor. Soc.,
861 99, 955–973. <https://doi.org/10.1175/BAMS-D-17-0014.1>, 2018.

862 Vernier, J. P., Fairlie, T. D., Natarajan, M., Wienhold, F. G., Martinsson, B. G., Crumeyrolle
863 S., Thomason, L. W., and Bedka, K. M.: Increase in upper tropospheric and lower
864 stratospheric aerosol levels and its potential connection with Asian pollution, J. Geophys.
865 Res., 120, 1608–1619, <https://doi.org/10.1002/2014JD022372>, 2015.

866 Visioni, D., Pitari, G., di Genova, G., Tilmes, S., and Cionni, I.: Upper tropospheric ice
867 sensitivity to sulfate geoengineering, Atmos. Chem. Phys., 18, 14867-14887,
868 <https://doi.org/10.5194/acp-18-14867-2018>, 2018a.

869 Visioni, D., Pitari, G., Tuccella, P., and Curci, G.: Sulfur deposition changes under sulfate
870 geoengineering conditions: QBO effects on transport and lifetime of stratospheric
871 aerosols, Atmos. Chem. Phys., 18, 2787-2808, doi: 10.5194/acp-18-2787-2018, 2018b.

872 Vogel, B., Müller, R., Günther, G., Spang, R., Hanumanthu, S., Li, D., Riese, M., and Stiller,
873 G. P.: Lagrangian simulations of the transport of young air masses to the top of the Asian

874 monsoon anticyclone and into the tropical pipe, *Atmos. Chem. Phys.*, 19, 6007-6034,
875 <https://doi.org/10.5194/acp-19-6007-2019>, 2019.

876 Wernli, H., Boettcher, M., Joos, H., Miltenberger, A. K. and Spichtinger, P.: A trajectory-
877 based classification of ERA-Interim ice clouds in the region of the North Atlantic storm
878 track, *Geophys. Res. Lett.*, 43, 6657–6664, doi:10.1002/2016GL068922, 2016.

879 Winker, D., Pelon, J., Coakley, J., et al.: The CALIPSO MISSION A Global 3D View of
880 Aerosols and Clouds. *Bull. Amer. Met. Soc.*, 91, 1211-1229, doi:
881 <http://dx.doi.org/10.1175/2010bams3009.1>, 2010.

882 Wu, G. X. and Zhang, Y. S.: Tibetan Plateau forcing and the timing of the monsoon onset over
883 South Asia and the South China Sea, *Monthly Weather Rev.*, 126, 913–927,
884 [https://doi.org/10.1175/1520-0493\(1998\)126<0913:TPFATT>2.0.CO;2](https://doi.org/10.1175/1520-0493(1998)126<0913:TPFATT>2.0.CO;2), 1998.

885 Yang, Y., Wang, H., Smith, S. J., Easter, R. C., and Rasch, P. J.: Sulfate aerosol in the Arctic:
886 Source attribution and radiative forcing. *J. Geophys. Res.*, 123, 1899–
887 1918. <https://doi.org/10.1002/2017JD027298>, 2018.

888 Yeh, S. W., Park, R. J., Kim, M. J., Jeong, J. I., and Song, C. K.: Effect of anthropogenic
889 sulphate aerosol in China on the drought in the western-to-central US, *Sci. Reports*,
890 5,14305, DOI: 10.1038/srep14305, 2015.

891 Yu, P., Murphy, D. M., Portmann, R. W., Toon, O. B., Froyd, K. D., Rollins, A. W., Gao, R.
892 S., and Rosenlof, K. H.: Radiative Forcing from anthropogenic sulfur and organic
893 emissions Reaching the Stratosphere, *Geophys. Res. Lett.*, 43, 9361–9367,
894 <https://doi.org/10.1002/2016GL070153>, 2016.

895 Yu, P., Rosenlof, K. H., Liu, S., Telg, H., Thornberry, T. D., Rollins, A. W., Portmann, R. W.,
896 Bai, Z., Ray, E. A., Duan, Y., Pan, L. L., Toon, O. B., Bian, J., and Gao, R. S.: Efficient

897 transport of tropospheric aerosol into the stratosphere via the Asian summer monsoon
898 anticyclone. P. Natl. Acad. Sci., 114, 6972–6977.
899 <https://doi.org/10.1073/pnas.1701170114>, 2017.

900 Zhang, Q., He, K., and Huo, H.: Cleaning China's air, *Nature*, 484, 161–162, 2012a.

901 Zhang, K., O'Donnell, D., Kazil, J., Stier, P., Kinne, S., Lohmann, U., Ferrachat, S., Croft, B.,
902 Quaas, J., Wan, H., Rast, S., and Feichter, J.: The global aerosol-climate model ECHAM-
903 HAM, version 2: sensitivity to improvements in process representations, *Atmos. Chem.*
904 *Phys.*, 12, 8911-8949, <https://doi.org/10.5194/acp-12-8911-2012>, 2012b.

905

906

907 Table 1: Details of model simulations performed.

908
909
910

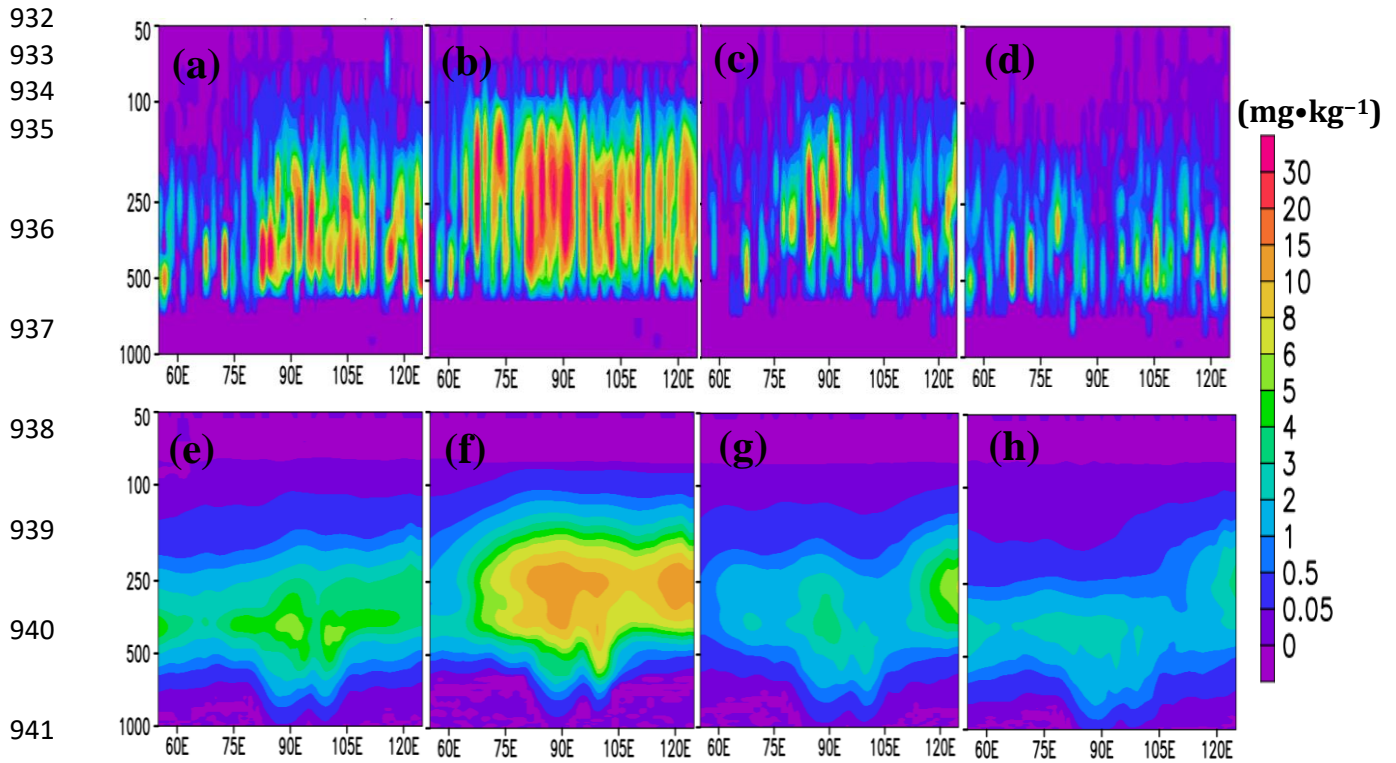
Sr. No	Experiment description	Name of experiment	SST and Sea Ice	Initial condition of the simulation	Analysis is performed for period
1.	Control simulation	CTRL	Monthly varying SST and Sea ice	1 – 10 January 2010	January – December 2011
2.	The anthropogenic emissions of SO ₂ over India (8 – 40°N; 70 – 95°E) are increased by 48%.	Ind48	Monthly varying SST and Sea ice	1 – 10 January 2010	January – December 2011
3	The anthropogenic emissions of SO ₂ over India (8 – 40°N; 70 – 95 °E) are increased by 48 % and reduced over China (23 – 45 °N; 95 – 130 °E) by 70 %.	Ind48Chin70	Monthly varying SST and Sea ice	1 – 10 January 2010	January – December 2011

911
912
913
914
915
916
917
918
919
920
921

922
 923 Table 2: Seasonal mean AOD in the UTLS (300 – 90 hPa) over India (75 – 95 °E; 20 – 35 °N)
 924 and Arctic (75 – 97 °E; 65 – 85 °N) from simulations performed. AOD is calculated at different
 925 altitude ranges indicated in brackets for some seasons since sulfate aerosol layer vary in altitude
 926 in the UTLS.
 927

Season	AOD in the UTLS over India from Ind48 (AOD*1E-04)	AOD in the UTLS over India from Ind48Chin70 (AOD*1E-04)	AOD in the UTLS over Arctic from Ind48 (AOD*1E-04)	AOD in the UTLS over Arctic from Ind48chin70 (AOD*1E-04)
Pre-monsoon	4.15 (4.17 %)	19.20 (19.25 %)	0.208 (0.017 %) (300–150 hPa)	2.09 (16.45 %)
Summer-monsoon	1.035 (2.17 %)	6.14 (12.9 %)	2.09 (2.14%)	-0.71 (0.073 %)
Post-monsoon	0.462 (3.03 %)	0.32 (0.61 %)	0.17(3.3 %) (100–50 hPa)	-0.4.9 (-5.8 %)
Winter	0.184 (1.1 %)	-1.01 (-6.62 %)	1.47 (4.8 %)	-2.3 (-7.79 %)

928
 929
 930
 931



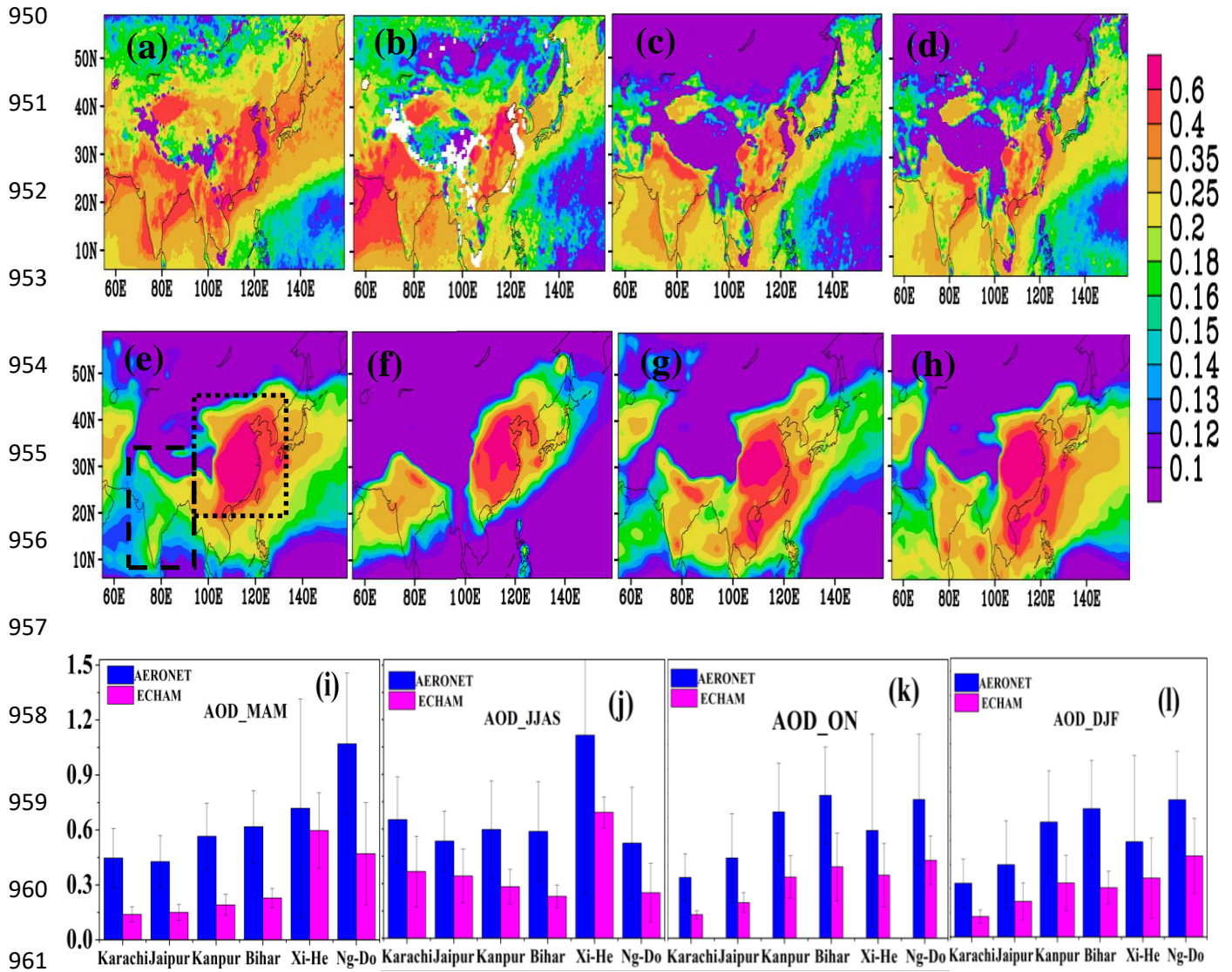
942 Figure 1: Seasonal mean distribution (2007 – 2010) of cloud ice mass mixing ratio ($\text{mg}\cdot\text{kg}^{-1}$)
 943 from CloudSat and CALIPSO combined 2C-ICE L3 averaged for 20 – 40 °N for the (a) pre-
 944 monsoon, (b) summer-monsoon, (c) post-monsoon, and (d) winter season, (e)-(h) same as (a)-
 945 (d) but from CTRL simulations.

946

947

948

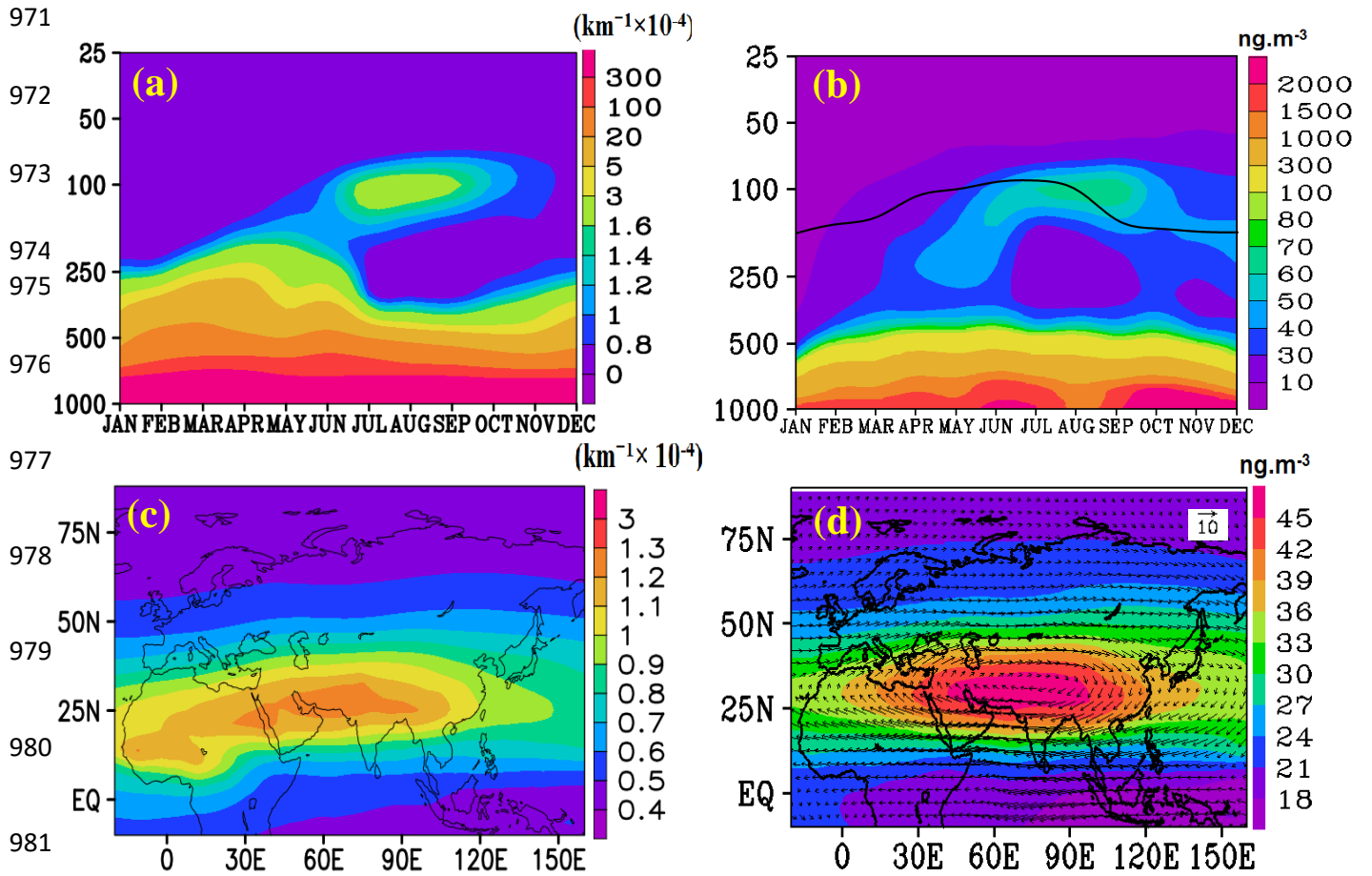
949



962 Figure 2: Seasonal mean Aerosol Optical Depth (AOD) from MISR (2000 – 2016) for the (a)
 963 pre-monsoon, (b) summer-monsoon, (c) post-monsoon, and (d) winter season, (e)-(h) same as
 964 (a)-(d) but from CTRL simulations, (i)-(l) same as (a)-(d) but from AERONET (2006 – 2016)
 965 at the stations: Karachi, Jaipur, Kanpur, Bihar, Xiang-He, Nghia-Do. The dashed box in Fig.
 966 (e) indicates the South Asian region (70 – 95 °E, 8 – 35 °N) where SO₂ emissions are
 967 enhanced by 48 % and the dotted box indicates Chinese region where SO₂ emissions are
 968 reduced by 70 % (95 – 130 °E; 20 – 45 °N).

969

970



982 Figure3 : Monthly vertical variation of (a) extinction ($\text{km}^{-1} \times 10^{-4}$) averaged for 70 – 120 °E,
 983 25 – 40 °N, (b) same as (a) but for sulfate aerosols ($\text{ng} \cdot \text{m}^{-3}$), (c) distribution aerosol extinction
 984 ($\text{km}^{-1} \times 10^{-4}$) at 100 hPa averaged for the summer-monsoon season, (d) distribution of sulfate
 985 aerosol ($\text{ng} \cdot \text{m}^{-3}$) at 100 hPa averaged for the summer-monsoon season. Wind vectors in Fig.
 986 (d) indicate extent of the anticyclone. Figs. (a)–(d) are obtained from CTRL simulations.

987

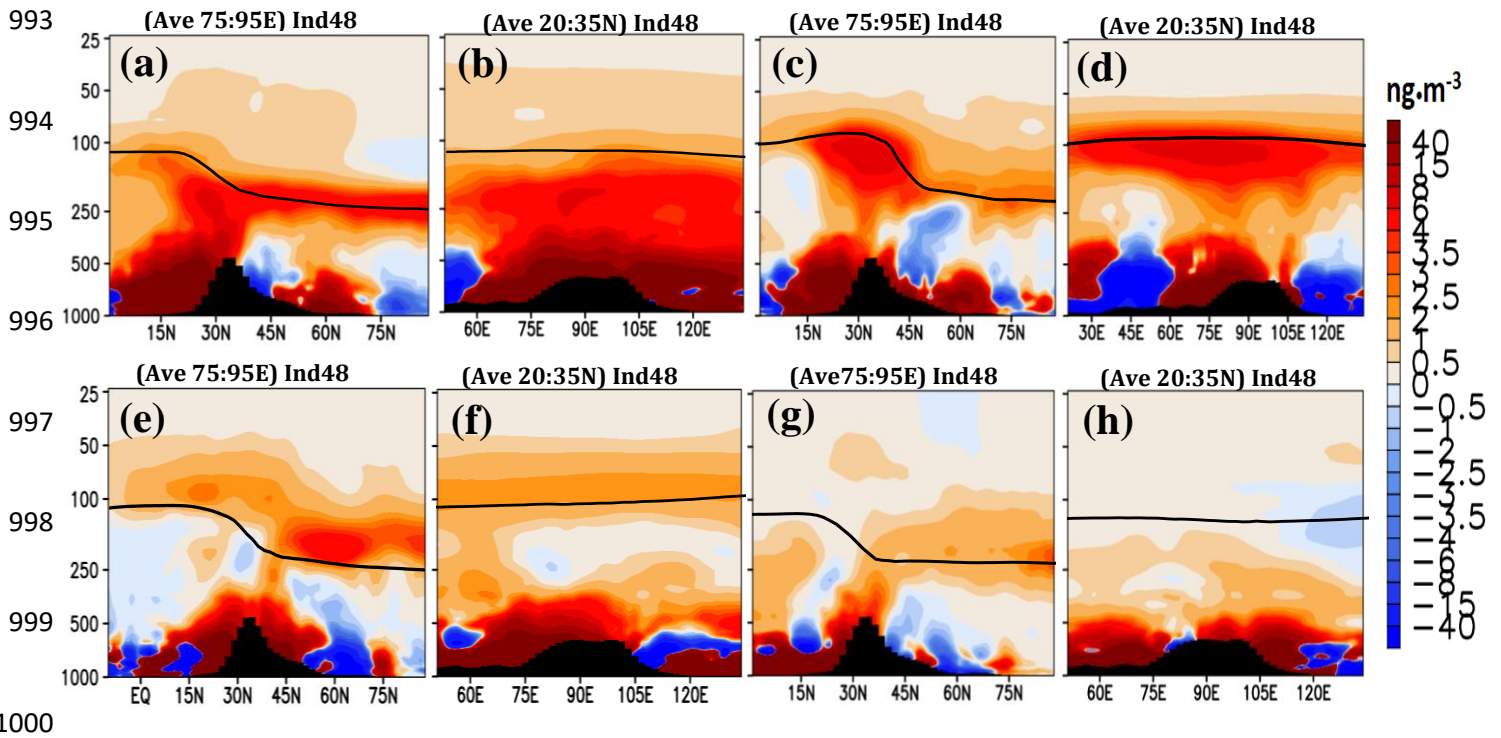
988

989

990

991

992

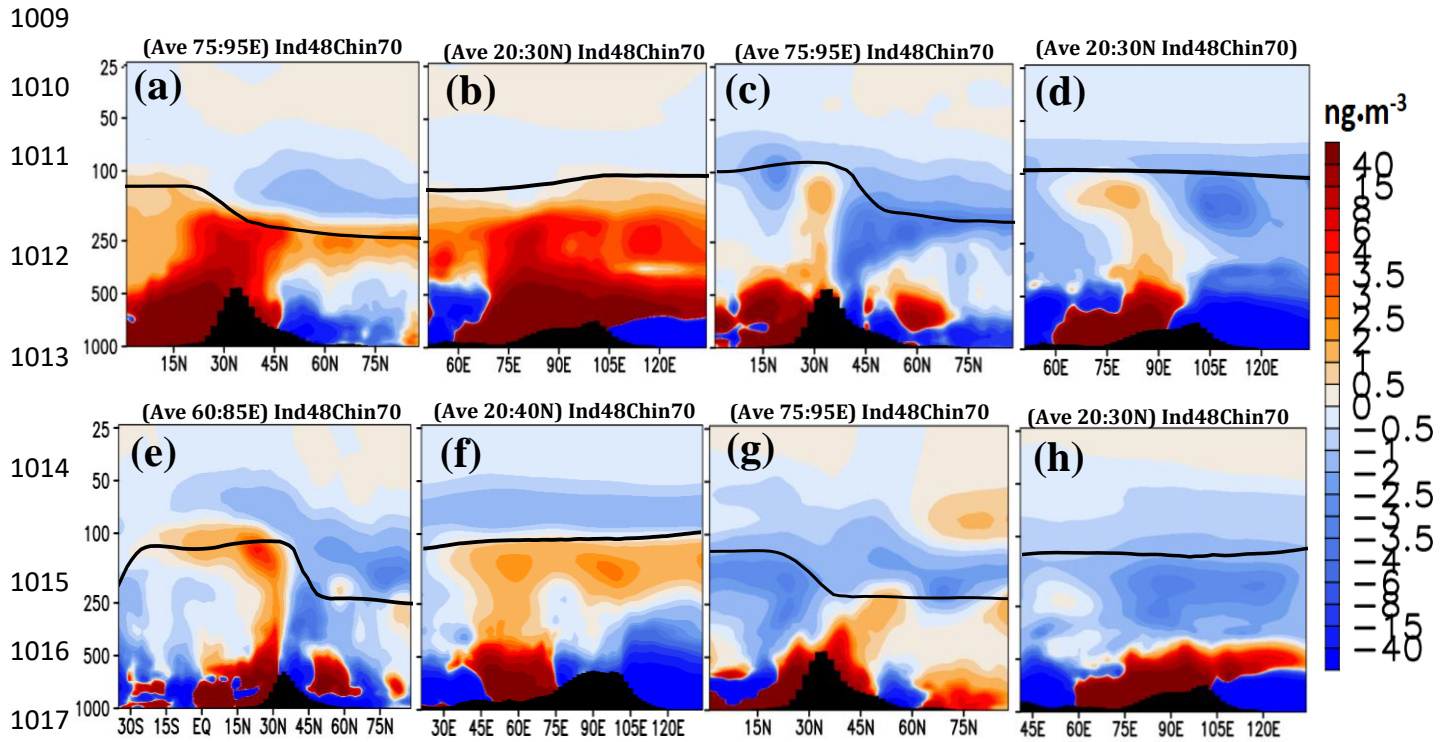


1000

1001 Figure 4: Vertical cross-section of anomalies in sulfate aerosols ($\text{ng}\cdot\text{m}^{-3}$) from Ind48-CTRL
1002 simulations for the pre-monsoon season (a) latitude-pressure section (b) longitude-pressure
1003 section, (c)-(d) same as (a)-(b) but for the summer-monsoon season, (e)-(f) same as (a)-(b) but
1004 for the post-monsoon season, (g)-(h) same as (a)-(b) but for the winter season. The averages
1005 obtained over latitudes or longitudes are indicated in each panel. The back vertical bars
1006 indicate topography and a black line indicates the tropopause.

1007

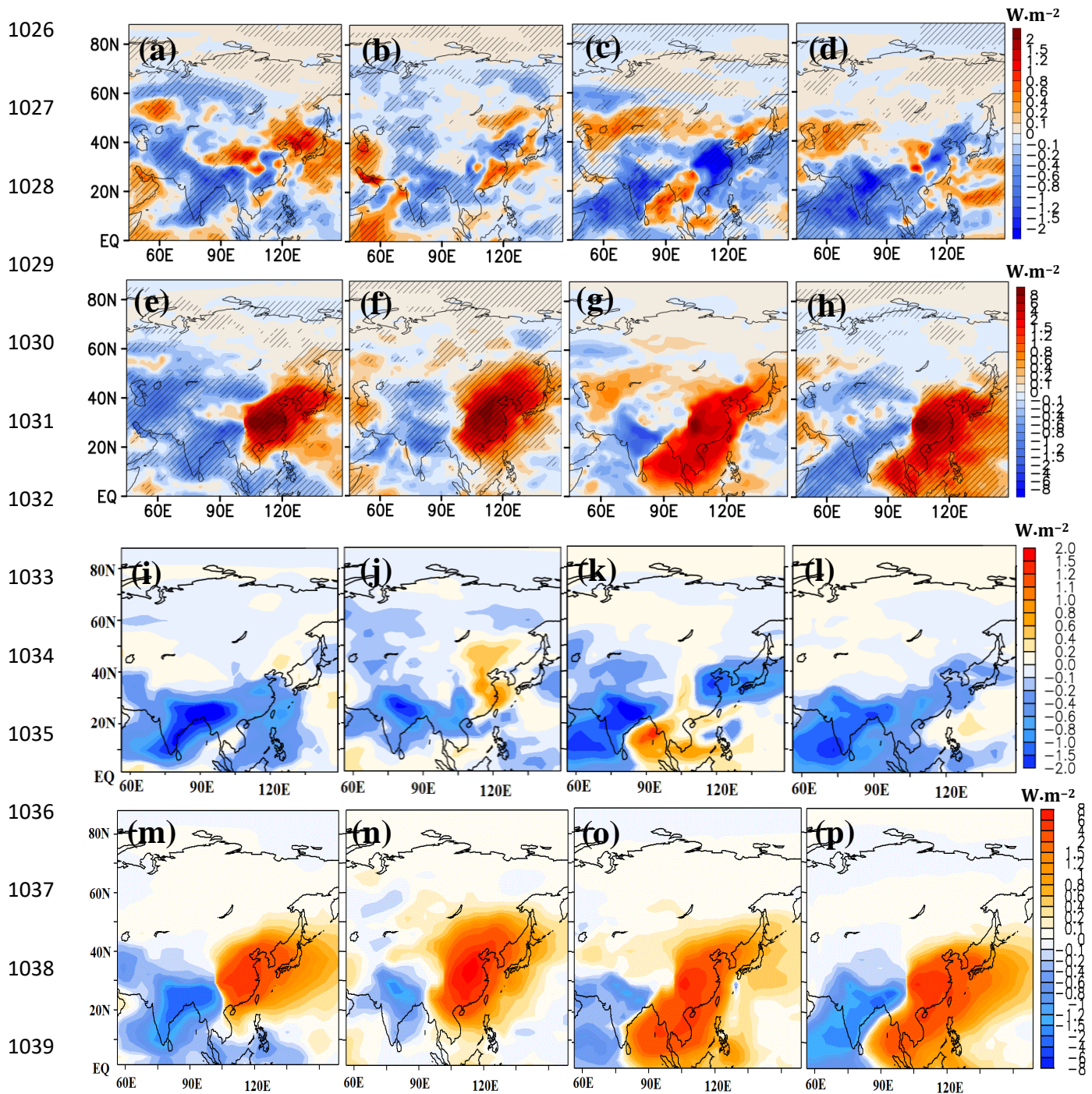
1008



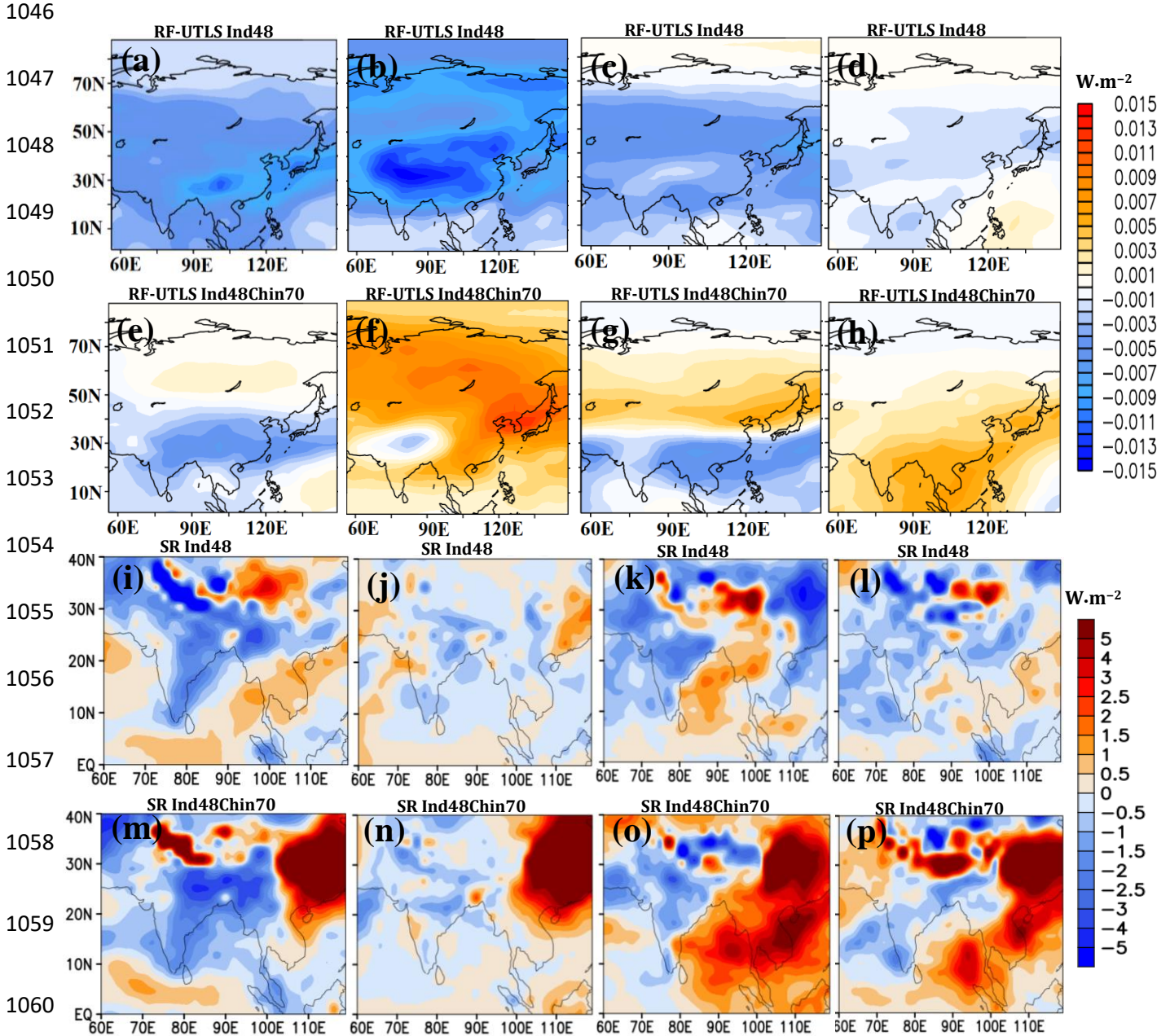
1018 Figure 5: Vertical cross-section of anomalies in sulfate aerosols ($\text{ng}\cdot\text{m}^{-3}$) from Ind48Chin70-
 1019 CTRL simulation for the pre-monsoon season (a) latitude-pressure section (b) longitude-
 1020 pressure section, (c)-(d) same as (a)-(b) but for the summer-monsoon season, (e)-(f) same as
 1021 (a)-(b) but for the post-monsoon season, (g)-(h) same as (a)-(b) but for the winter season. The
 1022 averages obtained over latitudes or longitudes are indicated in each panel. The back vertical
 1023 bars indicate topography and a black line indicates the tropopause.

1024

1025

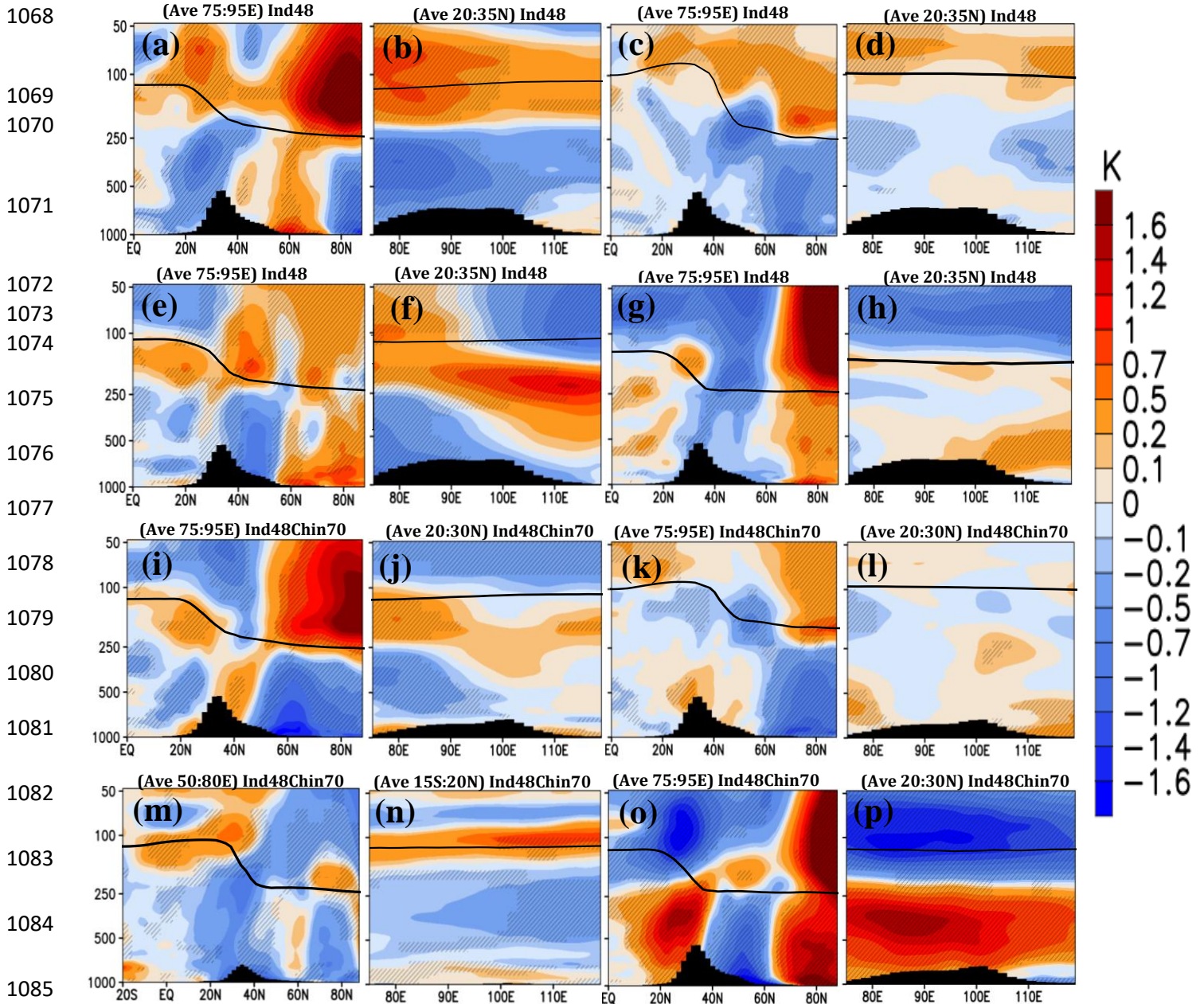


1040 Figure 6: Seasonal distribution of anomalies in clear sky direct **net radiative forcing** ($\text{W}\cdot\text{m}^{-2}$)
 1041 simulated by ECHAM6-HAMMOZ at the top of the atmosphere, from Ind48-CRTL
 1042 simulations for the (a) pre-monsoon (b) summer-monsoon, (c) post-monsoon and (d) winter
 1043 season, (e)-(h) same as (a)-(d) but from Ind48Chin70-CTRL simulations. (i)-(l) same as (a)-(d)
 1044 but from offline model, (m)-(p) same as (e)-(h) but from offline model. The black hatched
 1045 lines in Figs. (a)-(h) indicate the 99 % significance level.



1061 Figure 7: Simulated clear sky direct net radiative forcing at TOA ($W \cdot m^{-2}$) using the offline
 1062 model due to sulfate aerosols on the UTLS-only for the (a) pre-monsoon (b) summer-
 1063 monsoon, (c) post-monsoon, and (d) winter season for Ind48; (e)-(h) same as (a)-(d) but for
 1064 Ind48Chin70 simulations. Distribution of anomalies net solar radiation (SR) ($W \cdot m^{-2}$) at the
 1065 surface from Ind48 for the (i) pre-monsoon (j) summer-monsoon, (k) post-monsoon and (l)
 1066 winter season; (m)-(p) same as (i)-(l) but for Ind48Chin70 simulations.

1067



1086 Figure 8: Vertical cross-section of anomalies in temperature (K) from Ind48-CRTL
 1087 simulations for the pre-monsoon season (a) longitude-pressure section. (b) latitude-pressure
 1088 section, (c)-(d) same as (a)-(b) but for the summer-monsoon season, (e)-(f) same as (a)-(b) but
 1089 for the post-monsoon season, (g)-(h) same as (a)-(b) but for the winter season. Figures (i)-(p)
 1090 same as (a)-(h) but from Ind48Chin70-CRTL simulations. For the vertical cross-section
 1091 averages obtained over latitudes or longitudes are indicated in each panel. The black hatched
 1092 lines indicate the 99 % significance level. The back vertical bars indicate topography and a
 1093 black line indicates the tropopause.

1094

1095

1096

1097

1098

1099

1100

1101

1102

1103

1104

1105

1106

1107

1108

1109

1110

1111

1112

1113

1114

1115

1116

1117

1118

1119

1120

1121

1122

1123

1124

1125

1126

1127

1128

1129

1130

1131

1132

1133

1134

1135

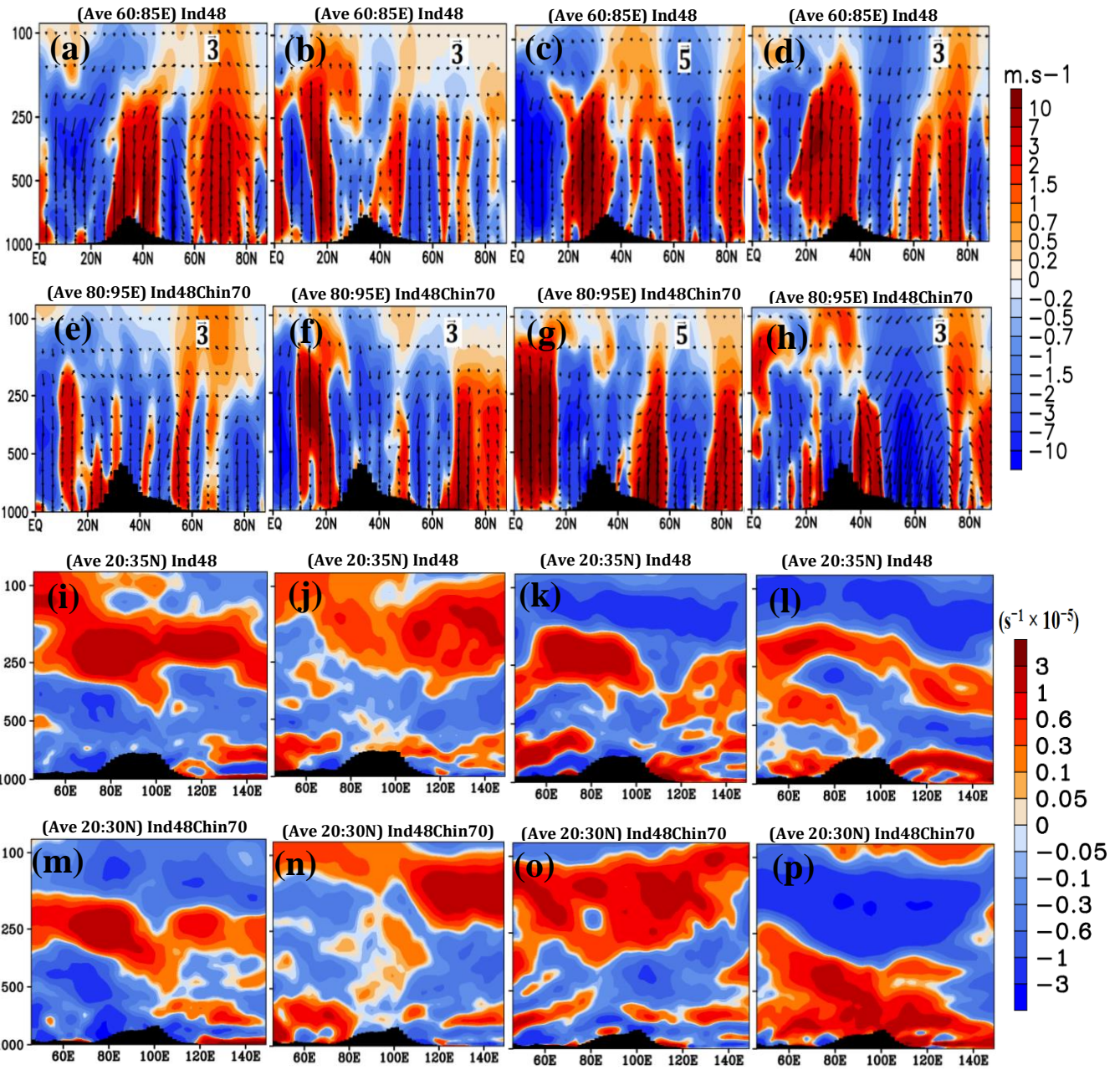
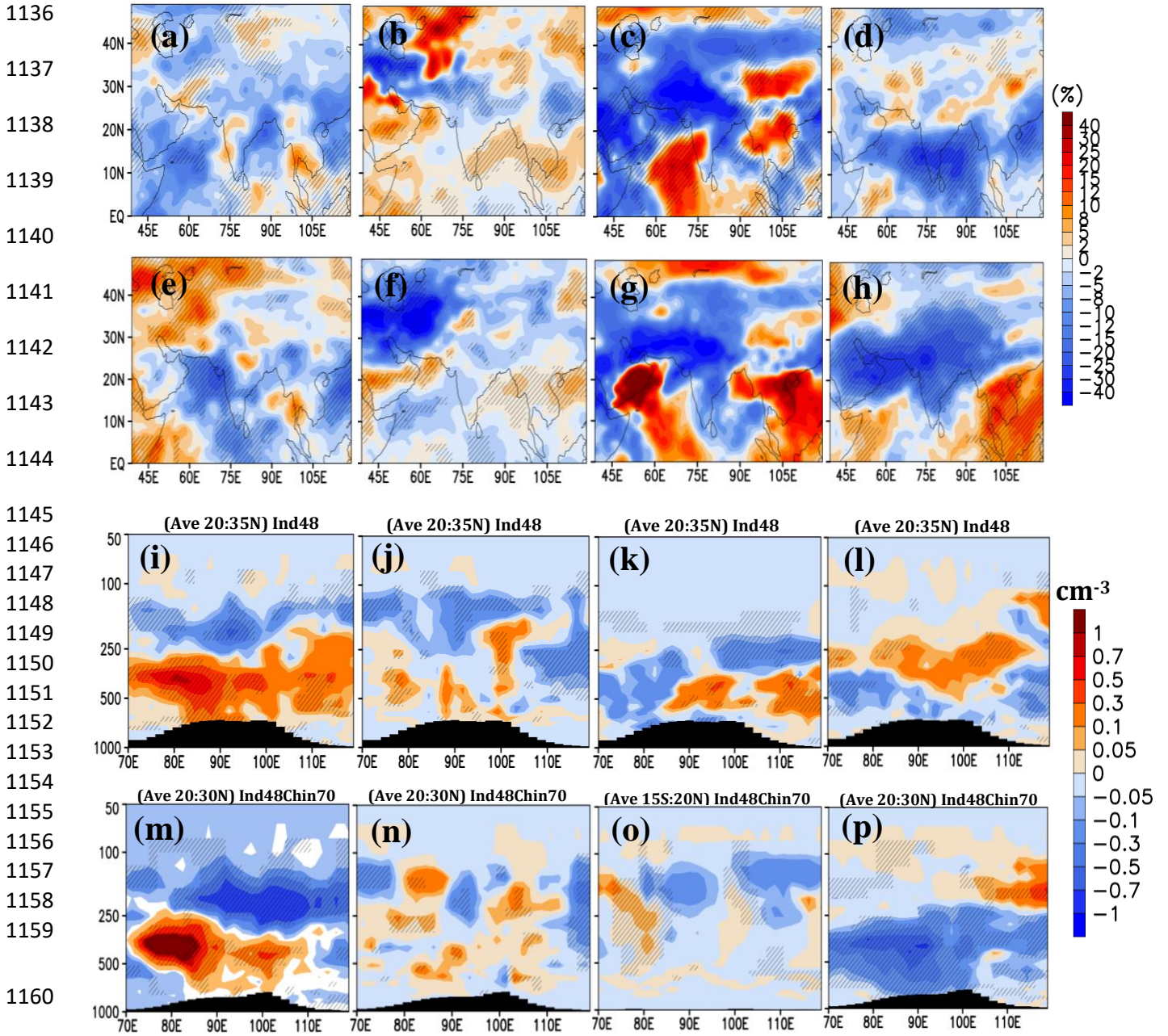


Figure 9: Distribution of anomalies in vertical velocity ($\text{m}\cdot\text{s}^{-1}$) from Ind48-CTRL for the (a) pre-monsoon (b) summer-monsoon, (c) post-monsoon and (d) winter season, (e)-(h) same as (a)-(d) but for Ind48Chin70-CTRL simulations. Vertical velocity is scaled by 1000. Seasonal distribution of anomalies in Brunt-Väisälä frequency ($\text{s}^{-1} \times 10^{-5}$) from Ind48-CTRL for the (i) pre-monsoon, (j) summer-monsoon, (k) post-monsoon and (l) winter season, (m)-(p) same as (i)-(l) but from Ind48Chin70-CTRL simulations. For the vertical cross-section averages obtained over latitudes or longitudes are indicated in each panel. The back vertical bars indicate topography.



1161 Figure 10: Seasonal distribution of anomalies in cirrus cloud (%) from Ind48-CRTL
 1162 simulations for the (a) pre-monsoon, (b) summer-monsoon, (c) post-monsoon, and (d) winter
 1163 season, (e)-(h) same as (a)-(d) but for Ind48Chin70-CTRL simulations, Seasonal distribution
 1164 of anomalies in ICNC (cm^{-3}) from Ind48-CRTL for the (i) pre-monsoon, (j) summer-monsoon,
 1165 (k) post-monsoon and (l) winter season, (m)-(p) same as (i)-(l) but from Ind48Chin70-CTRL
 1166 simulations. For the vertical cross-section averages obtained over latitudes or longitudes are
 1167 indicated in each panel. The black hatched lines indicate the 99 % significance level. The back
 1168 vertical bars indicate topography.